Aus dem Julius Wolff Institut
der Medizinischen Fakultät Charité - Universitätsmedizin Berlin

DISSERTATION

High-Resolution 3D-Characterization Reveals Distinct Phases of Cancellous Bone Formation in the Growing Murine Lumbar Spine

zur Erlangung des akademischen Grades
Doctor medicinae (Dr. med.)

vorgelegt der Medizinischen Fakultät
Charité - Universitätsmedizin Berlin

von

Herrn Michael Zenzes

aus Neuss

Datum der Promotion: 17.09.2021

Table of Contents

List of Abbreviations

General Abbreviations

C57BL/6	inbred strain of laboratory mice, 'Black 6'
d	days
EtOH	ethanol
g	gram
L3/ L4 / L5	third / fourth / fifth lumbar vertebral body
keV	kilo electron volt
µA	micro ampere
µCT	micro-computed tomography
µm	micrometer
mm	millimeter
Mp	megapixel
PBS	phosphate buffered saline
PFA	paraformaldehyde
PMMA	polymethyl methacrylate
R^2	coefficient of determination
SD	standard deviation
VOI	volume of interest
2D	two dimensional
3D	three dimensional

Specific Abbreviations related to 3D-Measurements (Appendix A)

BV/TV	bone volume to tissue volume ratio
BS/BV	bone surface to bone volume ratio, specific bone surface
DA	degree of anisotropy
SMI	structure model index
Tb.Th	trabecular thickness
Tb.Sp	trabecular separation
Tb.N	trabecular number

Consecutive numbers label the figures and tables in the dissertation.

The original labeling and the reference [1] refer to figures and tables from the publication.

Abstract

Introduction: The spine plays a central role in the skeleton of all mammals with its geometry and structure being crucial for locomotion. As it is difficult to study in humans, mice have become an important alternative study model, widely used in skeletal research. In the murine spine, within the first two weeks of life, rapid, fundamental rearrangement of mineralized material takes place. However, skeletogenesis has mostly been studied only in 2D. In this work, I provide a detailed 3D quantification of the early structural evolution of the lumbar vertebra. This study describes the main growth processes leading towards the formation of load-bearing, mature cancellous bone architecture in the murine spine.

Methods: Ex-vivo samples were used to study the lumbar spine of young female C57BL/6 mice (1, 3, 7, 10, and 14 days after birth) using phantom calibrated, high-resolution 3D μCT, supported by 2D histological analysis and mapping.

Results: Three phases of cancellous bone growth were identified: During a templating phase, low mineral density material is deposited in poorly structured spicules. During a consolidation phase between day 1 and day 7, the material condenses and forms first struts while the structure begins to grow. Thereafter a phase of expansion commences beyond day 7, trabeculae reorient in space and accumulate higher mineral densities. By 14 days of age, the young lumbar spine exhibits all morphological features observed in the mature animal, suggesting that the structure is fully functional and load-bearing.

Conclusion: Cancellous bone of the spine evolves through spatial rearrangement of mineralized material in three phases: Templating, rearrangement, and expansion. This occurs in parallel with the development of locomotive abilities. Understanding of physiological cancellous bone development lays the foundation for future studies of short- and long-term pharmaceutical, metabolic, endocrinological, and mechanical effects on mineralized tissue as well as tissue healing and regeneration.

Kurzfassung

Einführung: Die Wirbelsäule spielt eine zentrale Rolle im Skelett aller Säugetiere, da ihre Geometrie und Aufbau entscheidend für die Fortbewegung sind. Auf Grund der Schwierigkeit von Untersuchungen am Menschen, sind Mäuse zu einem wichtigen alternativen Studienmodell geworden, das in der Skelettforschung weit verbreitet ist. In der Wirbelsäule der Maus findet innerhalb der ersten zwei Lebenswochen eine rasche, grundlegende Umlagerung von mineralisiertem Material statt. Die Skelettentstehung wurde bislang jedoch meist nur in 2D untersucht. In dieser Arbeit biete ich eine detaillierte, 3D-Quantifizierung der frühen Strukturentwicklung der Lendenwirbelsäule. Diese Studie beschreibt die zentralen Wachstumsprozesse, die zur Bildung einer belastbaren, reifen, trabekulären Knochenarchitektur in der Wirbelsäule der Maus führen.

Material und Methodik: Ex-vivo Proben wurden verwendet, um die Lendenwirbelsäule von jungen, weiblichen C57BL/6 Mäusen (1, 3, 7, 10 und 14 Tage nach der Geburt) anhand von phantomkalibrierter, hochauflösender 3D μCT, zu untersuchen, unterstützt durch histologische 2D-Analysen und Darstellungen.

Ergebnisse: Es wurden drei Phasen des trabekulären Knochenwachstums identifiziert: Während einer Vorlagenphase wird Material mit geringer Mineraldichte in wenig strukturierten Partikeln abgelegt. Während einer Konsolidierungsphase zwischen dem ersten und siebten Tag verdichtet sich das Material und bildet erste Verstrebungen, währen die Struktur zu wachsen beginnt. Im Anschluss beginnt eine Expansionsphase nach Tag sieben, in der sich die Trabekel im Raum neu orientieren und höhere Mineraldichten akkumulieren. Im Alter von 14 Tagen weist die Lendenwirbelsäule alle morphologischen Merkmale eines ausgewachsenen Tieres auf, was darauf hindeutet, dass die Struktur voll funktionsfähig und belastbar ist.

Schlussfolgerung: Trabekulärer Knochen der Wirbelsäule entsteht durch die räumliche Neuanordnung von mineralisiertem Material in drei Phasen: Vorlage, Kondensation und Expansion. Dies geschieht parallel zur Entwicklung der motorischen Fähigkeiten. Das Verständnis der physiologischen Entwicklung von trabekulärem Knochen bildet die Grundlage für zukünftige Untersuchungen der kurz- und langfristigen pharmazeutischen, metabolischen, endokrinologischen und mechanischen Auswirkungen auf mineralisiertes Gewebe sowie auf die Knochenheilung und Regeneration.

1. Introduction

1.1. Bone: Material and Tissue

Bones consist of a rigid, mineralized material that forms the skeleton in all vertebrates and mammals [2]. Bones protect inner organs, take part in the mineral homeostasis, house bone marrow, which is essential for the production of blood cells, while playing a central role as a supporting structure in locomotion [2–4]. Bones are organized in two tissue types: (i) Compact bone, a solid, typically tubular structure on the outer cortex of bone, provides resistance to bending and an insertion point for tendons and muscles. (ii) Cancellous bone, an elaborate, porous architecture, absorbs and transfers load inside the wrapping of the cortical bone [2]. During growth, bones undergo radical changes in structure and material properties, as a load-bearing architecture emerges, that is adapted to sustain load associated with locomotion. Bones - as a result of evolution and adaptation - match their specific location and function [4]. This is reflected by their overall shape and design: Long bones, e.g. femur or tibia, contain a tubular shaft with a diaphysis formed by compact cortical bone that encloses the bone marrow. Cancellous bone is found adjacent to the articular regions, in the metaphysis and epiphysis. Irregularly shaped bones, e.g. vertebra, consist of a round vertebral body (centrum) which is filled with a dense network of cancellous bone. The vertebral body is surrounded by a shell of cortical bone and dorsally spanning vertebral arches with their cranial and caudal articulations (Figure 1). Each vertebral body has a unique shape and size, adapted to its position within the vertebra.

Bone comprises a homeostatic network of bone-forming and -resorbing cells, namely osteoblasts, osteocytes, and osteoclasts [4–6]. Osteoclasts, derived from hematopoietic monocytes, secrete proteolytic enzymes that break down the mineralized matrix and form cavities. Osteoclasts are necessary for bone resorption and shaping during growth, remodeling, and repair. Osteoblasts, which are of mesenchymal origin, produce bone proteins, orchestrate mineralization, and fill cavities formed by osteoclasts. Osteocytes, derived from osteoblasts, form a mechanosensitive syncytium with osteoblasts and lining cells on the bone surface. They are located within the bone matrix and interconnected by a network of canaliculi. Osteocytes control structure integrity and play a central role in the strain-dependent organization of remodeling by modulating osteoclast activity to ensure a balanced process of bone resorption and formation [7,8]. Common to all bones is the material they are made of: A natural composite of proteins (collagen type 1, osteocalcin, osteonectin, osteopontin) and mineralized particles (hydroxyapatite) that form a complex, hierarchical ‘plywood’-like structure from a nanometer length scale up to the macroarchitecture

of bone size and shape [2,3,5,9]. The bone material is geared to provide optimal mechanical support while using up minimal mass [2].

Up until the end of puberty the process of bone growth, shaping, and mineralization can be described as ‘modeling’, a parallel activation of bone-forming and -resorbing cells; whereas the lifelong coordinated turnover, repair, and adaptation of bone material as an interplay of its cellular components is referred to as ‘remodeling’ [10,11].

1.2. Physiological Osteogenesis: Cells, Mineral and Strain

Bones form through the process of calcification, a highly regulated, carefully balanced process of biomineralization. Bone formation originates from ossification centers, created during embryogenesis [12–14]. There are two types of ossification mechanisms, namely endochondral and intramembranous ossification. Both are delicately orchestrated, and their underlying cellular and molecular mechanisms have been studied in great detail [4,5,12,15–25]. During intramembranous ossification, bone develops directly from mesenchymal cells through the mineralization of type-1 collagen; no cartilage is present [4,20]. During endochondral ossification, bone forms through the replacement of a cartilaginous anlage of chondrocytes that proliferate, undergo hypertrophy, and mineralize, leaving a scaffold of mineralized cartilage that is invaded by vessels as well as bone-forming and -resorbing cells [4,15,20,22,24,25]. Bone forming cells appear to follow a ‘scaffold-like’ primary tissue of extracellular matrix during the deposition of mature bone [26]. Bone grows by the apposition of material to existing surfaces; this may be endosteal, periosteal, endochondral, or perichondral (on the surface of mineralized cartilage) [2,5,27]. A growth plate forms between the primary ossification center (diaphysis) and the secondary ossification center (epiphysis) [28]. It hosts proliferating and hypertrophic cartilage. During puberty, under the influence of hormones, the growth zone is narrowed and bridged by the ossification front, resulting in a fusion of the ossification centers and termination of longitudinal growth [4].

Collagen orientation in the extracellular matrix of bone rearranges during growth. Woven bone shows an irregularly arranged pattern and has poor mechanical properties [29]. This can be seen for example in rapidly formed fetal bone. Woven bone is then remodeled into lamellar bone with its matrix arranged in layers and improved mechanical competences [2,29]. Struts and forming trabeculae reorient in space during early development and maturation: Starting from a radial pattern, they approach a latter-like configuration [1,30].

Bone is a result of biomineralization. The mineral mainly consists of hydroxyapatite crystals, varieties of calcium phosphate [2,4,24]. During ossification and growth, the mineralized material is distributed to the narrow growth zone via closely related, partially open vessels through mineral containing vesicles, stored in granules inside osteoblasts. The vessels secrete granules to mineralize the extracellular matrix [9,19,24].

Bone continuously adapts to mechanical strain and stimuli, as was already suggested by Julius Wolff and has been elaborated since [2,31–33]. Genes and signaling cascades control the fundamental shape of bone intrinsically, whereas strain and mechanical stresses caused by muscles, appear to be predominant factors that shape the developing bone - already during embryogenesis [2,28,31,34–36]. Muscle forces regulate chondrocyte intercalation in columns; continuous compression increases cartilage cell proliferation, while intermitted compression inhibits proliferation [34,35]. Maintenance of shape and proportions during growth is achieved by isometric scaling, a fine balance of growth rates in different growth plates [37]. A lack or absence of mechanical stimulus leads to delayed ossification and affects both bone formation and architecture [34,38].

1.3. Bone Quality: Architecture Shaped by Movement

Bone quality is determined by the mutual influence of bone architecture, material composition, and mechanical demands [2,3,9,11,39,40]. The development of bone quality proceeds rapidly during the first few days of life [1].

Mature cancellous bone develops a complex network of trabeculae as a result of material maturation and continuous adaptation. The mechanical properties of this architecture can be described by the degree of mineralization and fabric structure, namely the degree of anisotropy [2,11,33,40,41]. Vertical trabeculae are supported by horizontal trabeculae that deflect strain from one vertical strut to another [2,30]. Vertically applied compressive stress tends to bend and fracture horizontal struts, while vertical trabeculae seem to absorb energy through bending and micro-cracks, allowing to maintain overall structure [42,43]. Micro-cracks are repaired through remodeling, which is achieved by biomechanical sensing of the osteocyte-osteoblast network and ensures adequate mechanical competencies that allow for transmission and absorption of mechanical stress [7,8,43]. Depending on the direction and mode of loading, it is non-trivial to estimate the forces, which act upon the cancellous bone, due to its non-homogeneous, anisotropic structure [2,33]. The cancellous bone of the spine contributes mostly to bone strength (resistance

to inelastic/plastic deformation), while it contributes less to the material stiffness (resistance to elastic deformation). Nevertheless, it has to be considered in the context of the cortical bone shell that surrounds it [2,44–48]. Intervertebral disks reorganize the multidirectional forces to a principal craniocaudal loading-axis, which is reflected by the increasing proportion of trabeculae following the loading direction [1,2,30]. The double-tube geometry of the round vertebral body and the circular vertebral arches enables the spine to be flexible and at the same time resistant to bending.

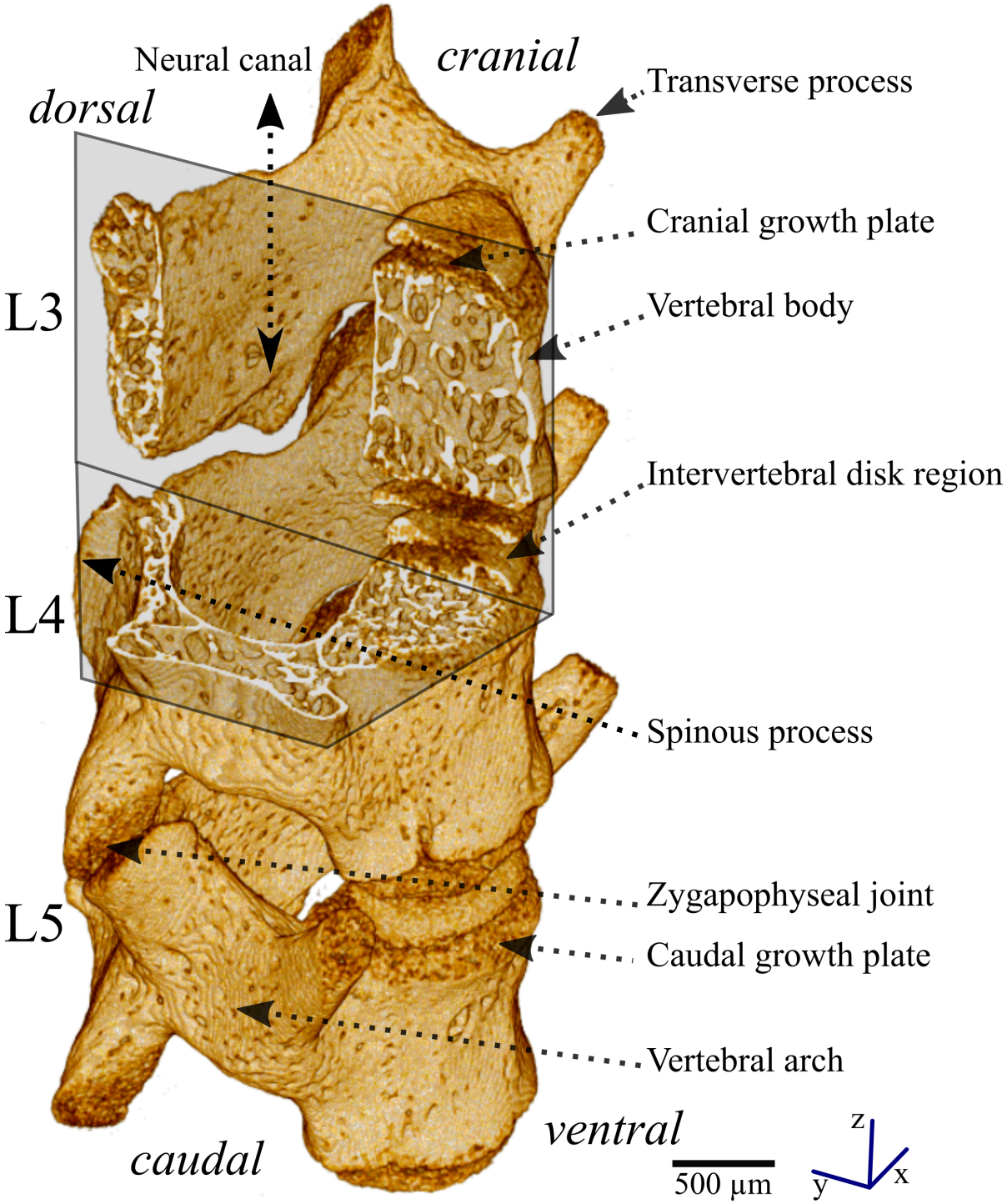

Figure 1: 3D rendering of a representative lumbar spine segment L3-L5 in a 14-day-old C57BL/6 mouse. Annotations describe selected anatomical landmarks. A cutting plane in L3 and L4 exposes the cancellous bone structure in the centrum, vertebral arches, and the intervertebral disc region. The vertebral column fulfills several functions: Support of the head, transfer of forces from the limbs to the body, and support of the viscera. In tetrapod, this is achieved by an arch-like curvature of the spine, bound by the ventral body wall musculature [2]. *Figure created by the author, based on his data.*

1.4. Cancellous Bone Maturation: State of the Art

Few comparable µCT studies focus on the evolution of cancellous bone or the lumbar spine in mice or rodents at a very young age. This lack of data may be due to the delicate sample size and demanding handling as well as in former times the lack of adequate high-resolution imaging. A study performed by Bortel et al. describes long bone maturation of the femur [49], while the cancellous bone formation of the vertebra remained poorly covered until this publication [1]. Most studies either focus on older ages, the decline of bone architecture, or investigate long bones [49–54].

Cancellous bone in the tibial metaphysis of C57BL/6 mice shows a 60% loss in BV/TV between 1.5 months and 2 years of age, characterized by a loss of trabeculae and connectivity [53]. Similar declines were shown for the cancellous bone of the lumbar vertebra in C57BL/6 mice, using histomorphometry [55].

Glatt et al. analyzed the cancellous bone architecture of the lumbar spine in C57BL/6 mice between 1 and 20 months of age, using µCT at a resolution of 12 µm. The highest BV/TV and Tb.N were observed around the end of puberty at 1.5-2 months of age, with a steady loss of bone volume thereafter. Female mice showed lower BV/TV than their male peers. Relative to the femur, the vertebrae showed less decline in cancellous bone parameters [51].

Buie et al. described architectural changes in the vertebra of female C57BL/6 mice between 6 and 48 weeks of age, using µCT at a resolution of 19 µm. They report a BV/TV of about 15% for a 6-week-old specimen with an increase of up to nearly 40% BV/TV after 4 months [52]. In comparison: 4-month-old C57BL/6 vertebral bodies, scanned and analyzed under the protocol applied in this study, only showed half the BV/TV reported by Buie et al. (Appendix C). Different

scanning resolutions, threshold applications, the lack of histological confirmation, and the hand-drawn VOI selection contribute to these differences.

A μCT study of trabecular architecture formation in the human spine by Acquaah et al. found similar patterns, regarding templating and consolidation of bone material between birth and 2.5 years of age, comparable to the findings of this study [1,56].

It appears plausible that - despite methodical differences - the general trends described by these studies are accurate: After a drop in bone substance observed in early life, an increase takes place during growth - especially during puberty - before a slow decline commences [1,51,52,57,58]. The temporal gaps in observation remain to be investigated.

1.5. Mice as a Model for Skeletal Research

Mouse models are a cornerstone of bone research. They allow to address fundamental research questions while sharing certain common properties with human bones (Table 1) [59]. Their embryological development is fairly well documented [13,14]. C57BL/6 mice have been widely employed in bone research for decades [1,31,49–54,60–64]. Genetically modified strains allow investigation of individual signaling molecules, pathways, or structural properties [65–68].

Table 1: Comparative table of skeletal properties in mice and humans (selected results adapted from [59]).

	Mice	**Humans**
Cervical vertebrae	7	7
Thoracic vertebrae	13	12
Lumbar vertebrae	6	5
Sacral vertebrae	4	5
Coccygeal vertebrae	27 - 31	4
Growth plates	Persist throughout life, in a dormant state	Present only during growth and development, disappear thereafter
Trabecular thickness	< 50 μm	100 μm

1.6. 2D Histology: Staining Connective Tissue

Fundamental principles of bone biology were discovered in the last centuries using optical microscopes and variations of histological slices [20,32,69]. Detailed measurements of classical

histology, as well as specific immunohistochemistry stains, are commonly used today [70,71]. Histological staining differentiates and highlights cellular and acellular structures by enhancing contrast. Processing of histological slices requires histological fixation, to preserve cell morphology and prevent deformation or disintegration [72]. Reportedly formalin fixation (PFA) could alter the mineral content and mechanical properties of bone [73,74].

1.7. 3D Micro-CT: Non-destructive Inspection of Bone

µCT allows non-destructive, hence, repeatable 3D imaging and has become a frequently used method to investigate mineralized materials [75–77]. µCT combines a large number of 2D radiographs from different rotation steps to reconstruct and compute 3D images [78]. It uses polychromatic X-rays for image acquisition, high energy electromagnetic radiation, emitted by an X-ray source [79]. The energy (E) of an X-ray depends on its frequency, namely $E = h*f$, (h = Planck's constant, f = frequency), whereas the wavelength (λ) is inversely proportional to the frequency: $\lambda = c/f$ (c = light velocity, f = frequency). The shorter the wavelength, the higher the energy [79].

X-rays interact with the sample in multiple ways: Beams travel through the object, get attenuated, reflected, or absorbed, depending on their energy [79]. These interactions cause the image as well as potential artifacts: Beam hardening, an imaging artifact of polychromatic X-rays, does affect the outer regions of the sample (here: bone and 'air'). It is due to the absorption of X-rays of lower energy: These are absorbed in the periphery when entering the bone, while higher energy X-rays pass through the bone mass. This leads to a false depiction of higher density values on the boundaries of a homogeneously dense object [79]. Sample size, structure, and geometry have a significant influence on the accuracy of density measurements [76,80].

Motion and vibrations create streaking and blurring artifacts. Other image artifacts are caused by defective or uncalibrated camera and detector elements: Such imaging errors persist over the entire series of images and cause artificial, concentric ring structures in the reconstructed image [79].

A robust scanning protocol is crucial for the experiment and strongly affects result accuracy [76,81,82]. The ratio of scanning resolution to the size of the targeted features should be considered: The larger the voxel compared to the 'feature of interest' the bigger the error (Figure 13). Multiple factors influence image resolution, such as camera properties, exposure times, distances from the X-ray source to sample and image detector, the rotation angle as well as the

number of image projections obtained per position [76,83]. In theory, one could always aim for the highest scan resolution, but available data storage and the time required should be kept in mind. Furthermore, artifacts become more frequent with increasing scan durations, e.g. motion artifacts, shrinking, and drying artifacts [79].

1.8. Image Segmentation: Separating Bone from Background Image Information

Image segmentation is a crucial step for computed image analysis. It defines boundaries and simplifies data. Image segmentation into fore- and background has been addressed in multiple ways from manual separation over manual global threshold selection to automated algorithms [84–89]. An optimal approach uses non-parametric data to calculate an ideal threshold. A realistic, reliable, and reproducible separation is achieved to facilitate image analysis and 3D measurements. Despite the existence of μCT imaging guidelines and because of the variety of algorithms available, image segmentation remains a delicate subject. It has to be adapted to a specific research question, ideally employing 2D histomorphometry as a standard [1,76,90,91].

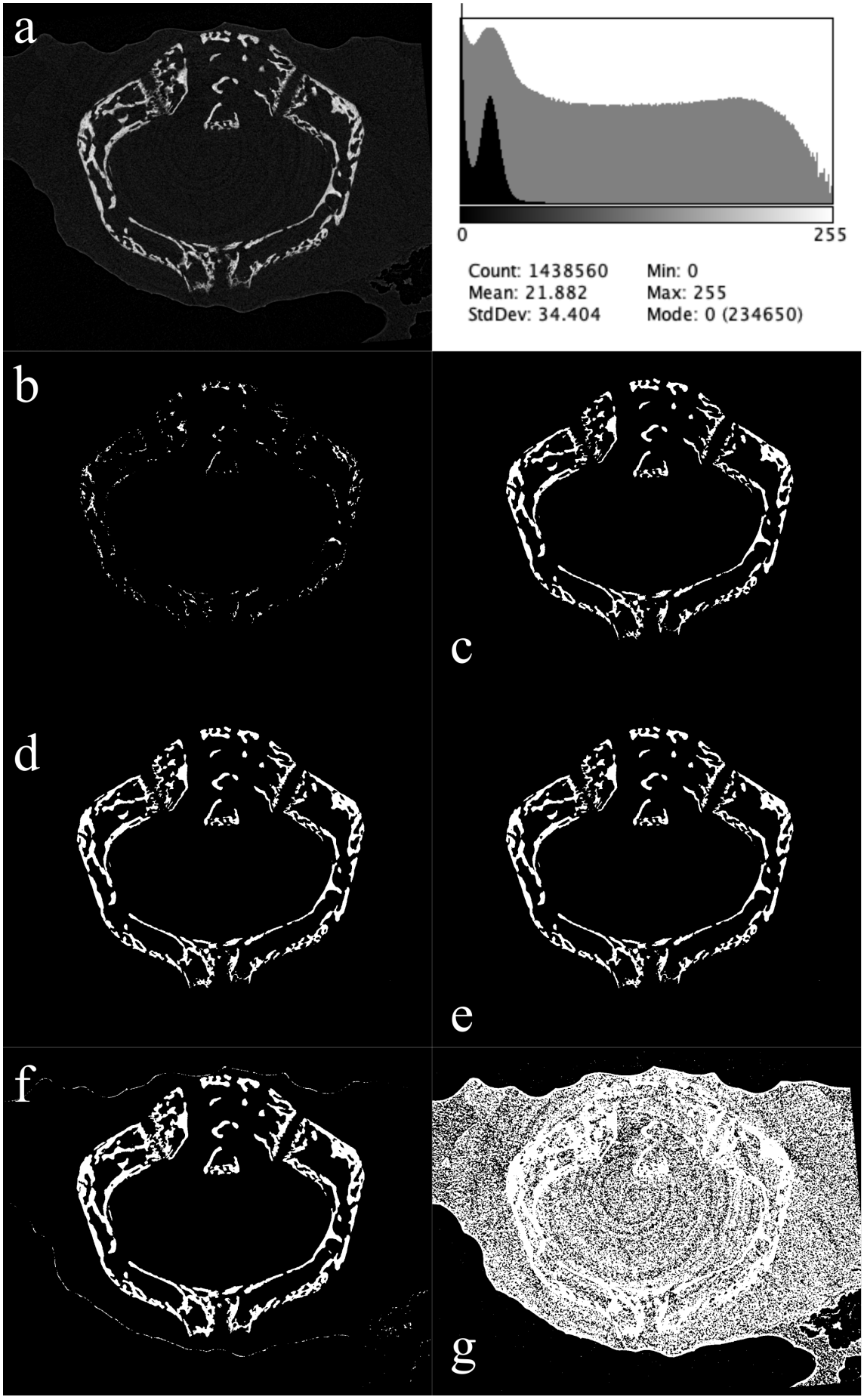
a
0
255
Count: 1438560
Mean: 21.882
StdDev: 34.404
Min: 0
Max: 255
Mode: 0 (234650)
b
c
d
e
f
g

Figure 2: Examples of different segmentation algorithms applied to a µCT image, sorted by their computed threshold level. **a** Representative transversal 8-bit grayscale µCT image of a 10-day-old mouse lumbar spine specimen and corresponding histogram. The bone of the vertebral body and arches show shades of gray, surrounded by soft tissue (gray) and an ethanol atmosphere (black). Very mild ring artifacts are present. The histogram shows a gray value distribution for each of the 1332 x 1080 pixels (= count of 1,438,560). Minimum = 0 (black), Maximum = 255 (white). The linear count is graphed in black with two peaks, showing an abundance of soft tissue and background in the unsegmented image. The logarithmic count in gray better represents the distribution of pixels at higher densities. **b** 'Shanbhag' calculates the "image as a compositum of two fuzzy sets corresponding to the two classes with membership coefficient associated with each gray level a function of its frequency of occurrence as well as its distance from the intermediate threshold selected" [92]. A cutoff at 202 is too high and only leaves a few high-density particles. **c** 'Intermodes' smoothens the histogram until it is bimodal and calculates a threshold as the middle of the two local maxima. In this example, it chooses a cutoff at 104, which is still relatively high [93]. **d** 'Default' segmentation algorithm in ImageJ is based on the isodata algorithm [94], it chooses an initial threshold which is then increased to be larger than the combined average of the two groups. A cutoff at 88 is very close to the threshold selected by Otsu's segmentation algorithm. **e** 'Otsu's' segmentation algorithm calculates a cutoff at 86. The algorithm aims to choose a threshold that maximizes the separability of two sections (fore- and background, bone and none-bone respectively), by using the discriminant criterion [85]. This threshold algorithm was used throughout this work [1]. **f** 'Yen' algorithm, a two-factor algorithm that employs cost functions to calculate a multilevel threshold, computes a relatively low cutoff at 49. [95] **g** The 'Percentile' algorithm uses a fixed fraction of foreground pixels at 0.5 and computes a very low cutoff at 16, which causes the inclusion of soft tissue [96]. *Figure created by the author, based on his data.*

1.9. Remaining open Questions

Bone growth at a very young age may seem trivial or well-known, but this period is poorly understood in detail. Most information is derived and extrapolated from 2D imaging and measurements. Comprehensive 3D data on the complex evolution of early cancellous bone formation were missing. The emergence of cancellous bone in the vertebra was lacking a description. The morphological transition from an immature, spongy template into a highly organized, load-bearing cancellous bone network was not examined. The influence of early locomotion on 3D structure formation and the implementation of mechanical demands by the spine

architecture were unknown. The redistribution of mineralized material during growth remains to be investigated [1].

1.10. Aim and Scope

The spatial and temporal evolution of cancellous bone has not been described in high-resolution and 3D yet. Little is known about the early postnatal period that hosts the transition from an immature mineralized structure to a fully functional spine architecture. It is substantial to comprehend its formation and geometric adaptation over time. To quantify the spine characteristics, a detailed examination of the development in a representative, well-studied model vertebrate was missing. The focus of this work is on the quantification of the structural and architectural evolution of cancellous bone in the murine lumbar spine [1]. This work provides a robust and defined series of protocols for sample handling and analysis, developed and applied to ensure reliable and reproducible characterization (Appendix B and E).

2. Materials and Methods

Figure 3 shows an overview of the samples and the different analysis methods applied.

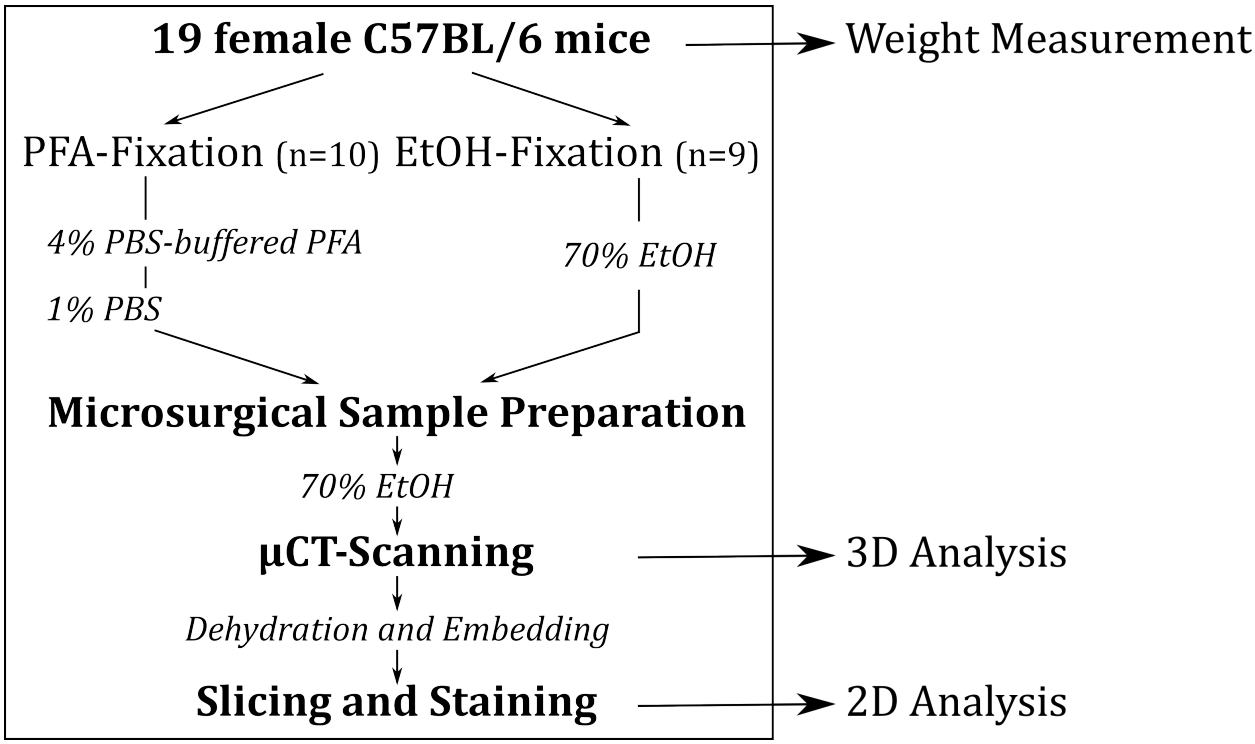

Figure 3: Flowchart of materials and methods. 19 female C57BL/6 mice, stored at -80 °C, were initially assigned to EtOH- or PFA-fixation. They were thawed during 24 hours at 4 °C in the respective medium. PFA-fixated samples were washed in PBS-solution for 2 hours. After microsurgical preparation (Figure 5) the extracted lumbar spine segments were stored in 70% EtOH at 4 °C until µCT-scanning (Figure 6). After the scan samples were returned to 70% EtOH until dehydration and PMMA-embedding. Samples were sliced and stained. See the Appendix for applied protocols. *Figure created by the author.*

2.1. C57BL/6 Mice: Microsurgery, Micro-CT, and Histological Preparation

19 healthy, female C57BL/6 mice pups at five timepoints within the first 14-days post-partum (n = 4 for 1, 7, 10, 14 days; n = 3 for 3 days), were obtained from litters at the Max Planck Institute of molecular genetics, Berlin, Germany (Figure 4) [1,49]. The study was designed to be based on a homogenous sample population to eliminate the possible influence of sex hormones or different genetic backgrounds.

Mice were initially assigned to a PFA- or EtOH-fixation medium (Figure 3) [73,74]. This initial subdivision was abandoned since there were no distinguishable differences neither in sample handling nor in µCT data. This is most likely due to the small sample size and the lack of effect of

PFA on the mineral content in the experimental setup. To preserve the delicate, small lumbar spine - a succession of hard and soft materials of different densities and properties - a Technovit 9100 new PMMA embedding was applied that allowed the samples to be non-decalcified (Appendix F). Movat's Pentachrome staining, a combination of different staining methods, allowed to differentiate mineralized bone and cartilage (Figure 10, Appendix H) [97]. Von Kossa / Toluidine Blue staining contrasts mineralized tissue in black and cartilaginous tissue containing proteoglycans and glycosaminoglycans in metachromatic shades of blue (Figure 11, Appendix G) [72].

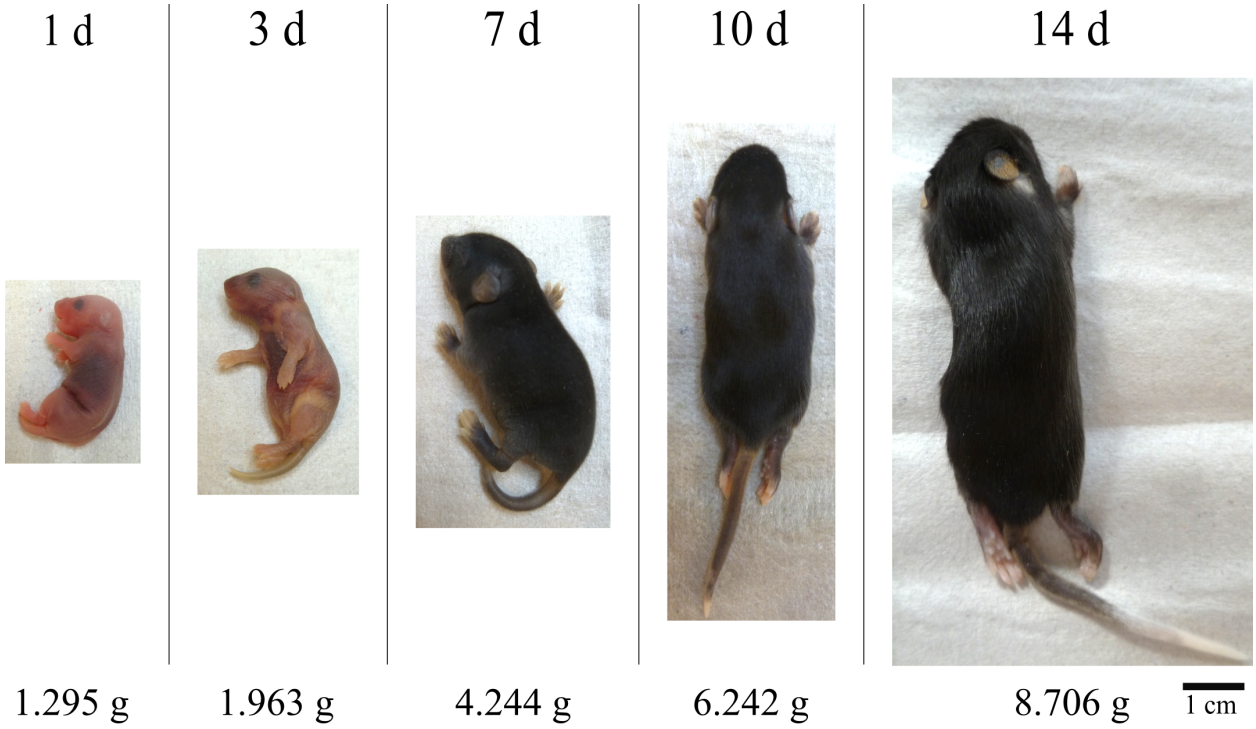

Figure 4: Scaled images of representative female C57BL/6 mice between 1 - 14 days post-partum. Average body weight per age-cohort in gram. The 1-day-old animal is pink and hairless, weighing slightly over 1 g. The 3-day-old animal is larger. First hints of pigmentation are present and ears begin to develop. At 7 days, the body is strongly pigmented and covered by short fur. The weight has tripled since birth. During the following 7 days, the fur thickens, mice increase in size, and double their weight. *Figure created by the author, based on his data.*

Lumbar spine segments were extracted micro-surgically under a stereomicroscope (x 2.5 magnification) since it is difficult to identify different vertebral regions by the naked eye in young animals (Appendix E) [1].

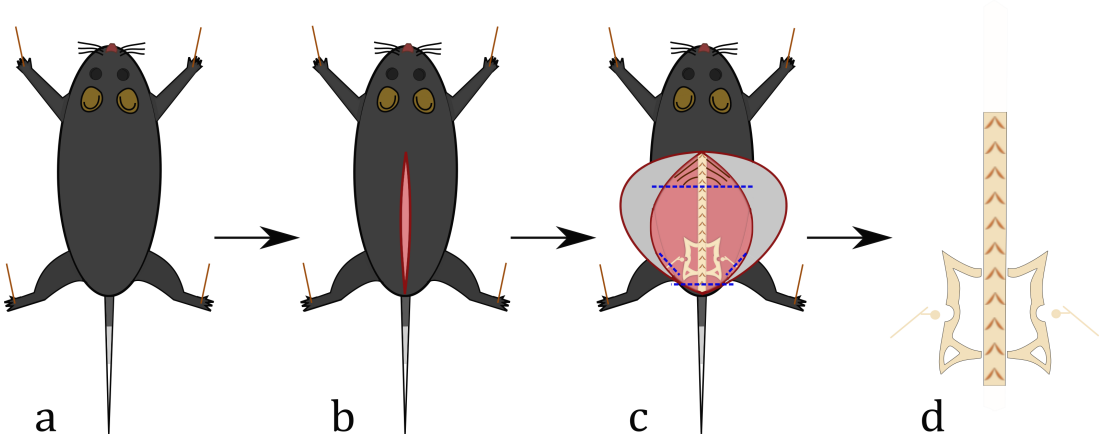

Figure 5: Microsurgical sample preparation (Appendix E) **a** Mice were carefully fixated on a polystyrene board with fore- and hindlimbs extended, avoiding strain. **b** A paravertebral incision was preferred for younger animals to avoid direct pressure on the spine. A medial incision was performed in animals 7 days and older. **c** Subcutaneous tissue and longitudinal paravertebral muscles were bluntly removed. Dotted lines indicate cuts for the extracted vertebral segment. In younger animals, the vertebral segment should be cut with a scalpel since scissors would crush the spine's macroarchitecture. **d** Extracted vertebral segment: Lumbar spine, pelvic bones, and proximal parts of the femur were extracted to minimize strain on the lower lumbar spine segments. *Figure created by the author.*

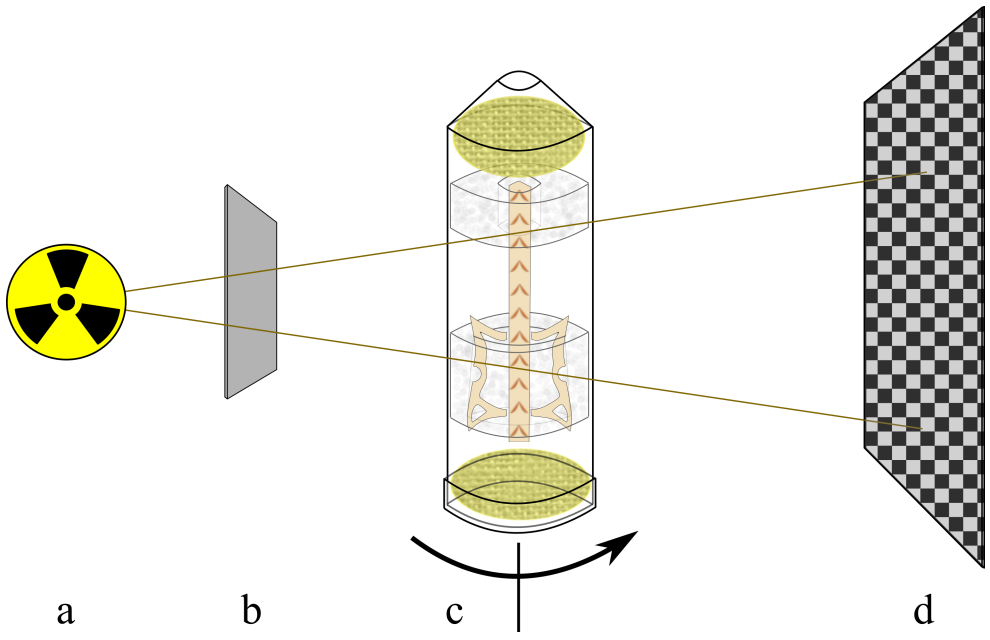

Figure 6: Skyscan Benchtop µCT 1172 setup (Bruker Micro-CT, Kontich, Belgium). **a** X-ray source (Hamamatsu 100/250); Object to source distance = 40.07 mm. **b** 0.5 mm aluminum filter, to reduce beam hardening. **c** Sample mounted in a custom-made specimen holder containing the polyethylene tube with the vertebral segment centered by two polystyrene rings. Plastic sponges

soaked in 70% EtOH ensure a constantly humid environment to prevent shrinking artifacts. **d** Camera (Hamamatsu C9300 11Mp camera); Camera to source distance = 277.528 mm. *Figure created by the author.*

All scans were performed using the same configuration for image acquisition to ensure comparability, resulting in a pixel size of 2.5 µm (Appendix B) [1]. The region of interest (vertebral bodies L3-L5) was selected after a scout scan before the 7 - 14 hours scanning process [1]. Filters in the scanning setup (Figure 6), as well as post-imaging correction algorithms, aimed to reduce beam hardening. The small size of my samples, as well as the lack of thick cortical bone surrounding the region of interest, further reduces the chance of significant beam hardening effects. The phantom calibrated, algorithm corrected µCT data highlight the mineral densities in growing bone [1,76].

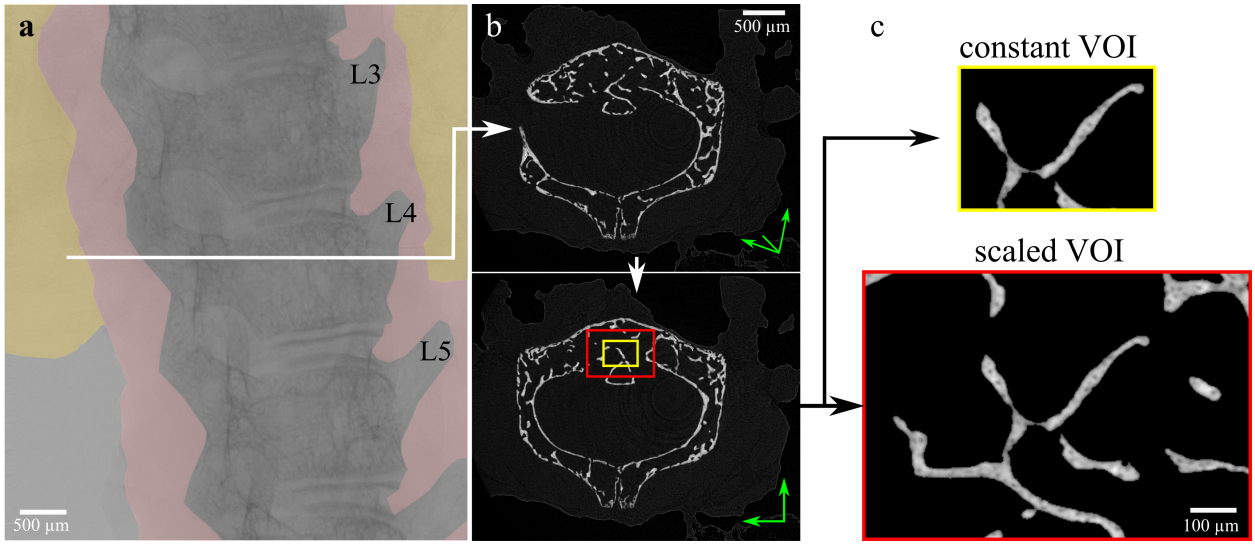

Figure 7: Image processing steps from µCT images to cleared VOI datasets. **a** µCT X-ray image from a representative 14-day-old animal; vertebrae L3-L5; red: soft tissue; yellow: shadow of the polystyrene ring (Figure 6); white line: location of b. **b** Reconstructed 2D µCT-slices (NRecon), before (top) and after (bottom) axial reorientation. **c** Cleared slices of the scaled and constant VOI with an indication of origin shown in yellow and red [1]. *Figure created by the author, based on his data.*

2.2. Image Analysis: From 2D to 3D

The image reconstruction software employed in this study (NRecon, v. 1.6.8.0, Bruker Micro-CT, Kontich, Belgium) uses the Feldkamp algorithm to transform the series of images into a data set of transversal images that allows further analysis [1,98]. Ring artifacts were reduced by the automated masking of defective pixels and a subsequent correction algorithm. To ensure a high

degree of comparability, identical settings for ring artifacts reduction, grayscale range, and beam hardening correction were applied to all samples during reconstruction. Mild misalignment correction was chosen for each sub-scan.

After testing and matching different segmentation algorithms with histological samples (Figure 2 and Figure 2 [1]), the non-parametric, user-independent Otsu's segmentation algorithm appeared most appropriate for samples of heterogeneous size and density. Otsu's segmentation algorithm was applied to each slice to separate bone from the background [1]. There is thus no universal, arbitrarily chosen threshold value. The segmentation algorithm was also used to 'clear' µCT slices from background information by creating a binarized mask [1]. An automated separation into the cancellous and cortical bone can be achieved using repetitive image processing and calculation steps (Appendix D). Two different VOIs were defined for improved comparability of 3D measurements: A small, constant VOI, comparable to the least common denominator, in the center of all vertebral bodies, and an adaptive scaled VOI to account for the volumetric increase during growth (Figures 7 and 8, Table 2) [1].

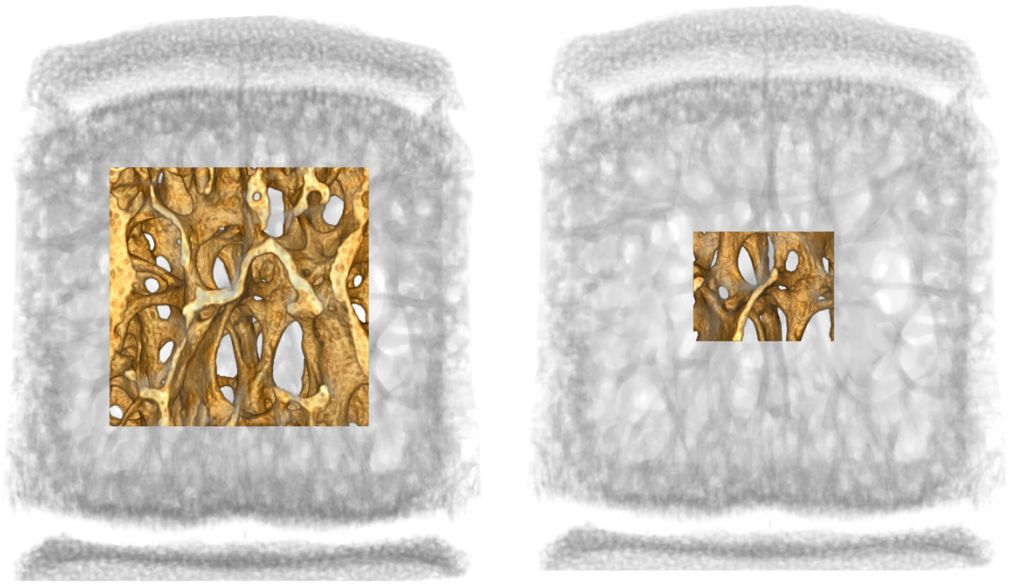

Figure 8: 3D model of the cancellous bone inside the scaled VOI (left) and constant VOI (right), highlighted in a 14-day-old vertebral body. Outlines of the vertebral body and growth plates are shown in gray (Figure 1 [1]). Scale bar = 500 µm. *Figure created by the author, based on his data.*

A wide range of 3D measurements were calculated in BoneJ, an ImageJ plugin [1,71,76,77,99–106]. 2D histomorphometric measurements were obtained and correlated to µCT (Figure 2). In addition to the rather conventional measurements, this study developed and applied additional

measurements of trabecular orientation, spatial and temporal evolution of mineral density, calibrated by phantoms of defined densities (Section 2.3 [1], Figure 6 [1], Figure 5h [1]). The effect of different scanning resolutions on 3D measurements was simulated to estimate the influence of lower image resolutions on the quantification of cancellous bone. The image pixel size of uncleared image sets was repeatedly halved to obtain virtual resolutions of 5 µm, 10 µm, and 20 µm. These images were then segmented using Otsu's segmentation algorithm and analyzed under the standard protocol (Figures 13 and 14).

3. Results

The high-resolution µCT data, matched by histomorphometry, reveals fundamental changes in bone morphology as well as cancellous bone architecture evolution during growth [1]. The vertebral bodies quickly increase in size and begin to elaborate anatomical features shown in Figure 1. These morphological changes are quantified in Figure 5 [1], while the temporal and spatial redistribution of mineralized material is exemplarily shown in Figure 6 [1].

3.1. Growth as a Function of Time and Weight

Dimensions of the growing lumbar vertebra are reported and graphed with the bodyweight of each animal since it allows to differentiate animals of the same age (Figure 3 [1]). The relation of age versus bodyweight in the animal cohort is linear, to an almost perfect R^2 fit (Figure 9). This suggests that it makes very little difference which parameter is presented in Figure 3[1].

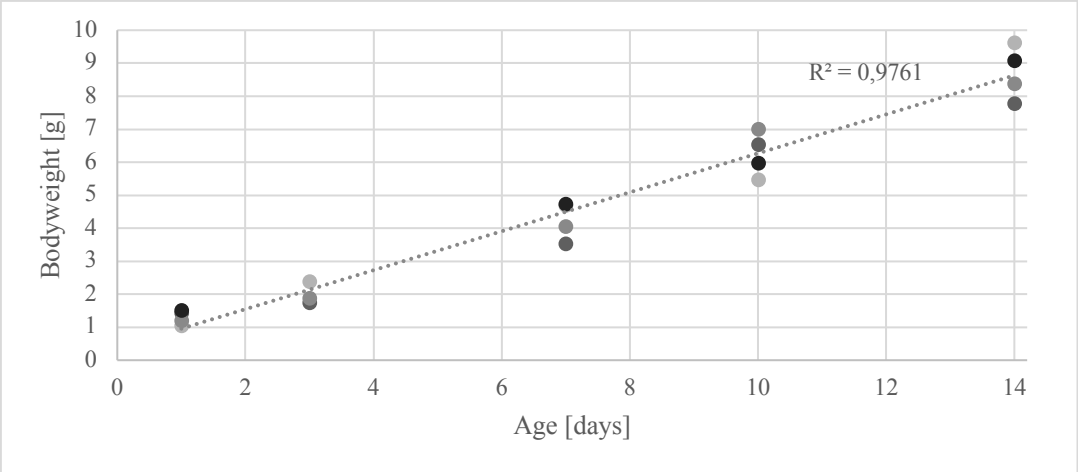

Figure 9: Graphed correlation (R^2) of age versus bodyweight with each data point corresponding to an individual animal. Data are given in full as a function of dimensions versus animal weight in Figure 3 [1]. *Figure created by the author, based on his data.*

The usual parameter used for comparative development studies is age since it is most practical in terms of monitoring developmental stages. Skeletal parameters in this study are given with respect to age, to ease comparison with other studies. However, both are plotted in Figure 3 [1], since both parameters improve extrapolation power and the quality of the fit at a very young age. The mathematical extrapolation of growth within the first two weeks, even allowed us to accurately predict the outer dimensions of a 4-month-old vertebral body [1] (Appendix C).

3.2. Evolution in Color: Histological Staining

The detailed results obtained in 3D were matched and confirmed by 2D histomorphometry at all timepoints. This ensures robustness and reliability for imaging and subsequent data analysis (Figure 2 and Table 1 [1]). Histological slices allow identifying the profound changes of the lumbar spine that occur during the early postnatal period. They add information on the cellular composition as well as the growth process outside the main region of interest.

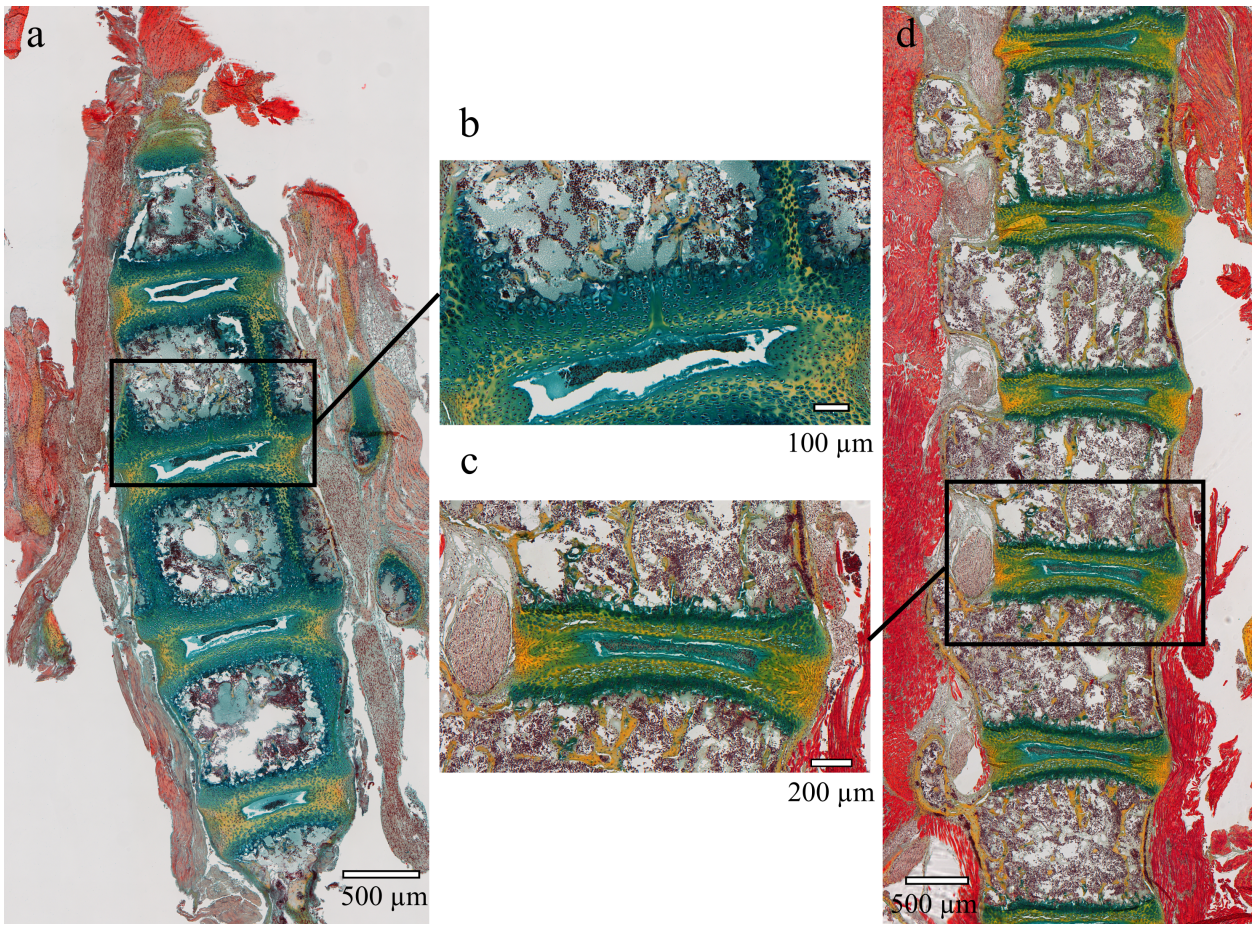

Figure 10: Movat's Pentachrome staining for 7 days (**a**) and 14 days (**d**). Magnifications of the respective growth plate region **(b)** and **(c)**. (Appendix H). Vertebral bodies are separated by intervertebral discs and growth zones on the cranial and caudal ends (dark shades of green and blue). **a** At 7 days, the mineralized cancellous bone (brown/yellow) is surrounded by a 'circular growth zone', a layer of cartilaginous cells, and mineralized cartilage (shades of green and blue) (**b**). Vertebral arches are separated by chondrogenic cells and are not yet fused with the vertebral body. **d** At 14 days, the gap between the vertebral body and the arches has closed. Only small islands of mineralized cartilage remain in that region. Cranial and caudal growth plates have narrowed. Small mineralized epiphyseal 'caps' have formed between the intervertebral discs and the growth zones (**c**) (Figures 1 and 11e). *Figure created by the author, based on his data.*

Developing bones contain bone and mineralized cartilage. My primary focus is however the former. Movat's Pentachrome staining shows that mineralized cartilage is mostly located on the periphery of the vertebral body, essentially in regions that were excluded from the scaled and constant VOIs (Figures 8 and 10) [1,97].

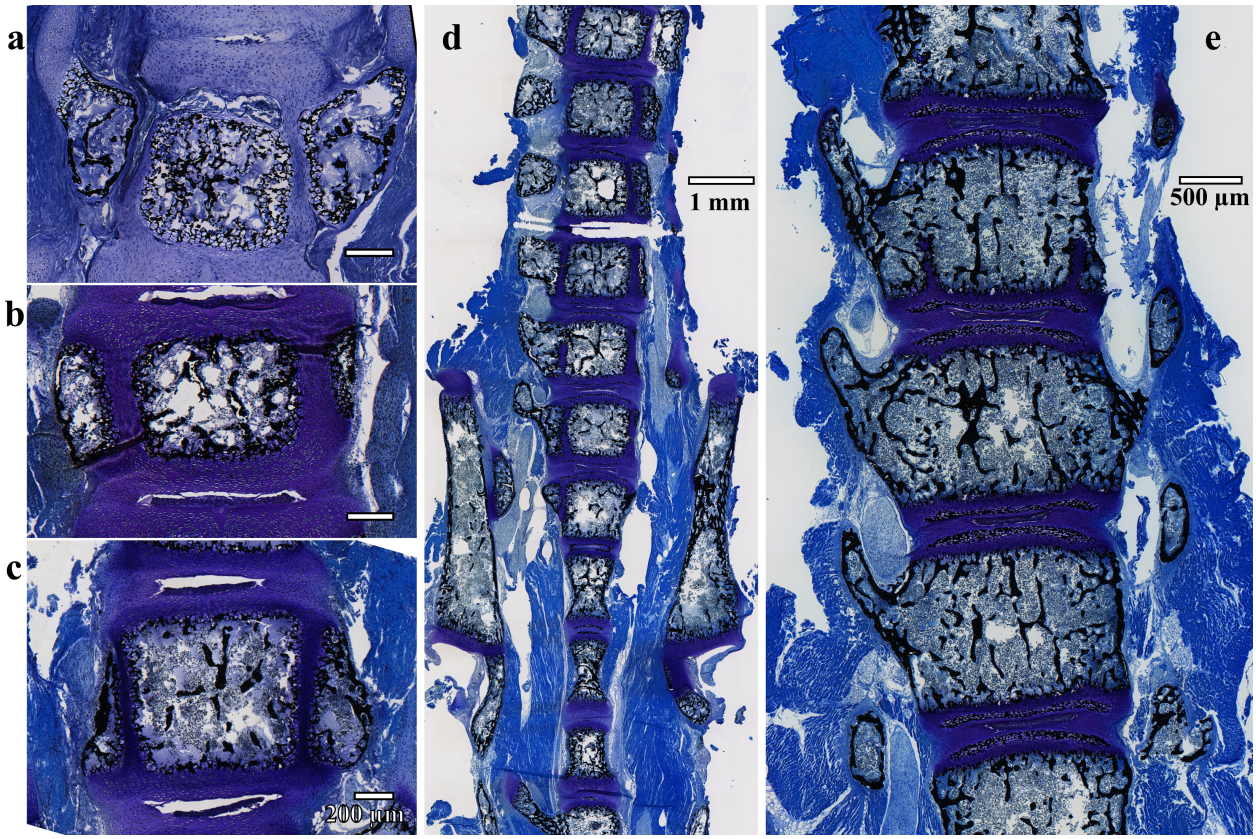

Figure 11: Von Kossa / Toluidine Blue staining of the lumbar vertebra from 1 - 14 days post-partum. Mineralized material (black). Chondrogenic tissue (metachromatic shades of blue). (Appendix G), scale bar a-c = 200 µm. **a** The 1-day-old vertebral body is a delicate network of mineralized spicules, surrounded by a layer of chondrogenic cells. The vertebral arches are pre-shaped in cartilaginous tissue. **b** At 3 days, the vertebral body shows signs of condensation in its center. It is still surrounded by an abundance of chondrogenic cells. **c** The 7-day-old vertebral body continues to consolidate mineralized spicules into struts and early trabeculae. The outer chondrogenic surface is thinning. **d** Overview of the lumbar spine, sacral spine, and hip bones, highlighting the anatomic complexity of this region at 10 days of age. The general trends continue and the vertebral bodies continue to grow. **e** At 14 days a nearly mature structure can be observed. Vertebral body and arches have fused. Von Kossa stains the mineralized epiphyseal 'caps' between the vertebral body and intervertebral discs in black. The growth zones are reduced to the cranial and caudal surface of the vertebral body (Figure 10 c, d). *Figure created by the author, based on his data.*

3.3. Cancellous Bone in two Volumes: The Center of Attention

Appropriate and constant selection of a VOI is essential for comparing multiple samples at different timepoints during growth, thus at different sizes [1,107]. The two VOIs introduced in the publication, show similar results (Table 2) [1]. This implies that they are both measuring similar structures and that the selection of the scaled VOI accurately excludes the peripheral growth zones, which adds to the accuracy of the 3D measurements and mineral density analysis.

Table 2: Constant VOI in relation to the scaled VOI (Figure 1[1]). Mean values (L3-L5) from 19 animals 1 - 14 days post-partum. BV/TV, Tb.Th, Tb.Sp, Tb.N, BS/BV, SMI, and DA are given including SD. To quantify the accuracy and comparability of different volumes, the correlation coefficient was calculated. Despite different volumes analyzed, a relatively high degree of correlation can be seen. The highest correlation was not found between the 1-day-old animals. This may be due to the fact, that the constant VOI could be slightly larger than the scaled VOI for the smallest animals at day 1, since it is based on the average size observed in 1-day-old animals [1]. *Table created by the author, based on his data.*

	Age {days}	**Constant VOI Mean**	Constant VOI SD	**Scaled VOI Mean**	Scaled VOI SD	**Correlation (r_{xy})**
BV/TV {%}	1	22.72	2.31	21.48	2.24	0.77
	3	15.99	2.79	16.78	2.07	0.90
	7	10.00	2.18	10.58	1.07	0.42
	10	11.31	1.86	11.65	1.38	0.72
	14	9.68	1.94	10.86	1.10	0.44
Tb.Th {µm}	1	16.87	1.33	16.45	0.89	0.69
	3	22.13	0.65	21.48	0.48	0.68
	7	27.82	2.60	26.20	1.28	0.73
	10	28.13	1.73	27.11	1.24	0.62
	14	30.30	2.03	28.82	1.54	0.82
Tb.Sp {µm}	1	74.80	12.41	76.79	12.99	0.92
	3	118.39	13.17	113.74	8.81	0.83
	7	190.24	36.55	167.31	19.48	0.52
	10	188.03	23.80	173.73	14.46	0.50
	14	225.00	29.90	193.95	19.05	0.26
Tb.N {mm^{-1}}	1	13.56	1.91	13.09	1.45	0.75
	3	7.25	1.36	7.82	0.96	0.88
	7	3.66	0.97	4.05	0.49	0.58
	10	4.02	0.59	4.31	0.55	0.56
	14	3.20	0.59	3.77	0.30	0.31

BS/BV {mm²/mm³}	1	3.412	0.095	3.275	0.151	0.52
	3	3.281	0.114	3.261	0.056	0.68
	7	3.024	0.172	2.998	0.115	0.80
	10	3.033	0.144	2.971	0.076	0.74
	14	2.834	0.158	2.806	0.114	0.60
SMI {}	1	2.998	0.183	3.077	0.258	0.58
	3	2.926	0.189	2.905	0.176	0.84
	7	2.914	0.307	2.863	0.130	0.62
	10	2.624	0.177	2.643	0.119	0.38
	14	2.549	0.191	2.438	0.113	0.50
DA {}	1	0.222	0.043	0.211	0.045	0.25
	3	0.250	0.067	0.213	0.075	0.51
	7	0.549	0.165	0.464	0.133	0.82
	10	0.408	0.143	0.504	0.073	0.02
	14	0.575	0.120	0.615	0.049	0.47

3.4. 3D Micro-CT: Morphology, Directionality, and Mineral Density

A panel of graphs highlights the changes in 3D measurements of cancellous bone architecture within the first two weeks of life (Figure 5 [1]). A drop in BV/TV is accompanied by a decrease in trabecular number, especially during the first 7 days (1). At the same time, trabecular structures become larger and more separated, indicated by an increase in Tb.Th and Tb.Sp. These changes are illustrated in 3D in Figure 12.

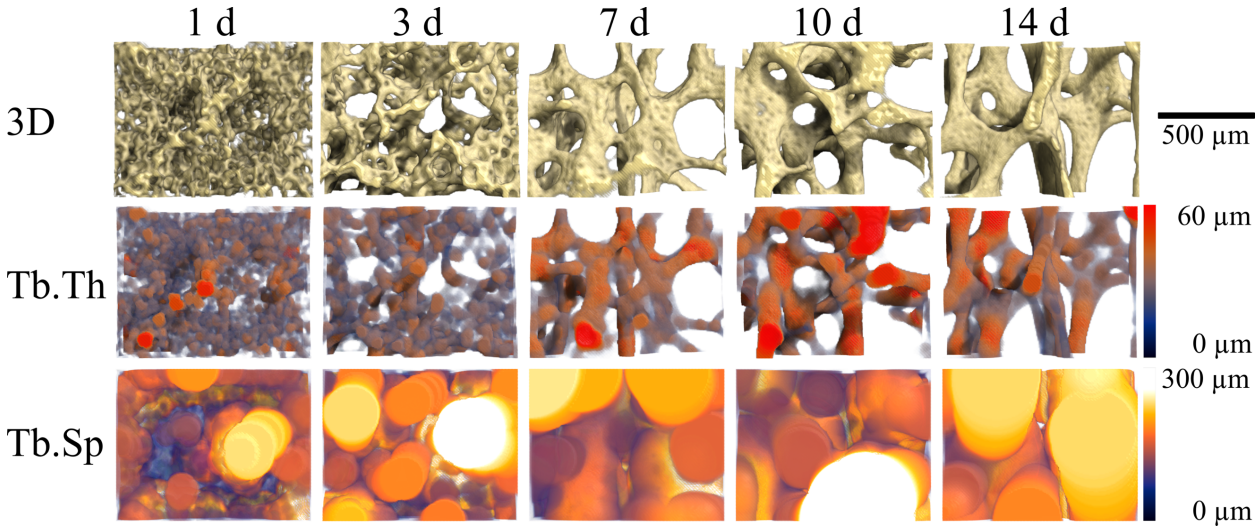

Figure 12: Quantitative 3D visualization of architectural evolution from 1 - 14 days post-partum (Figure 4 [1]). 3D surface reconstructions show the transition from a porous mineralized mass of spicules towards the formation of trabeculae. Trabecular thickness increases, especially at the intersection of vertical and horizontal trabeculae. Trabecular separation slowly increases over time, highlighted by orange and yellow 'bubbles' that represent cavities inside the cancellous bone.

Figure created by the author, based on his data. Adapted from Fig. 4 [1], by courtesy of Acta Materialia Inc; Elsevier Ltd.

Mineralized material approaches a preferred 'lattice'-like spatial orientation [1]. This is demonstrated by an increasing degree of anisotropy and a higher percentage of cranial-caudal oriented trabeculae (Figure 5g, h [1]). The material condenses into pillars, spanning the entire height of the vertebral body, supported by lateral struts (Figure 6a [1]). Mineral density increases over time, with a steady shift from densities below 1 g/cm^3 towards a peak around 1.4 g/cm^3, reflecting cancellous bone material maturation (Figure 6b [1]) [1].

The morphological changes observed in 3D, along with the patterns in trabecular orientation and anisotropy, as well as the temporal and spatial distribution of mineralized material provide a comprehensive analysis of physiological cancellous bone formation [1].

3.5. Effect of Image Resolution: Zooming out

The image resolution applied in this study was tested on histological samples and multiple test scans at different resolutions [1]. The resolution chosen here is sufficient to describe the development of mineralized architecture at a very young age. Higher resolutions were feasible but would require longer scan durations and a larger amount of data, hence, longer computing time at no justified yield of information. To analyze the effects of different image resolutions on 3D measurements and Otsu's segmentation algorithm, virtual image sets of lower resolutions were analyzed under the standard protocol.

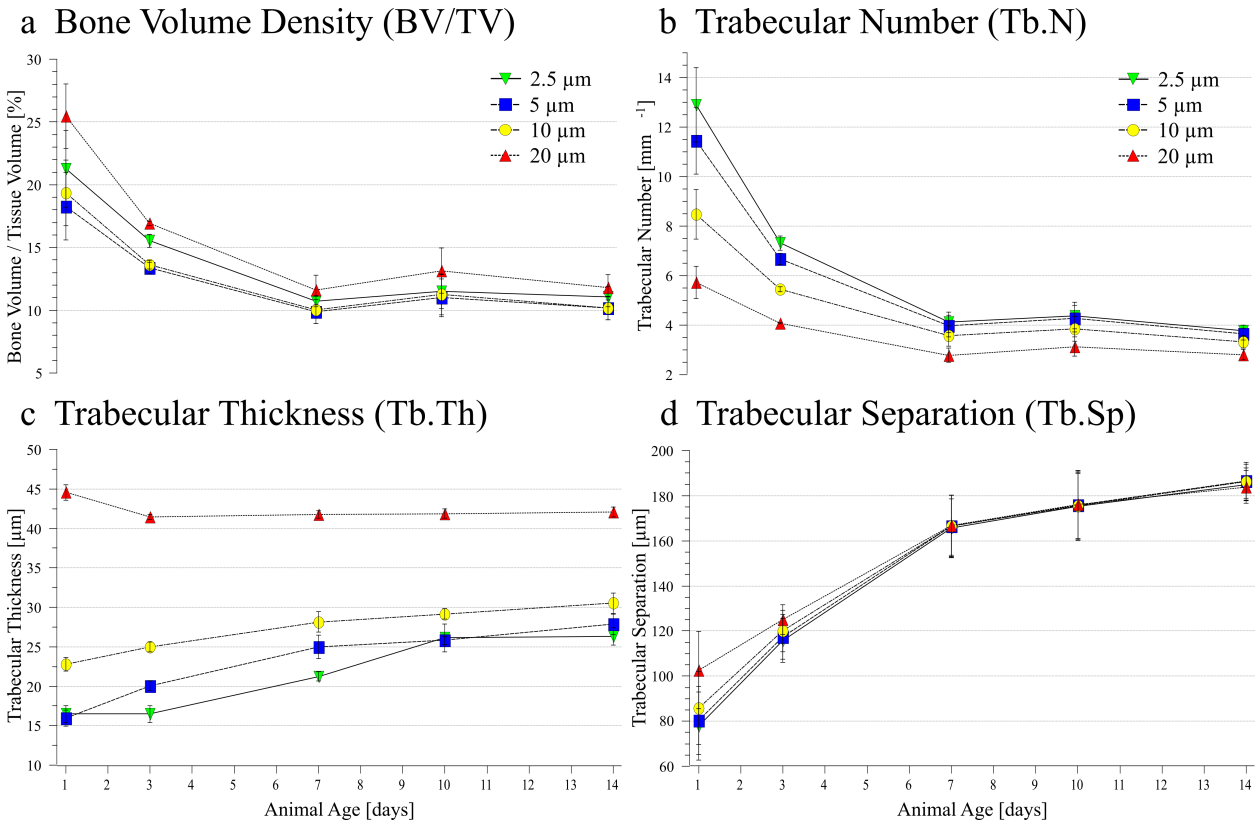

Figure 13: 3D measurements of simulated resolutions for pixel sizes of 2.5 µm (original resolution), 5 µm, 10 µm, and 20 µm (scaled VOI in L5 from 19 animals). The decreasing resolution has different effects. **a** BV/TV is slightly underestimated at pixel sizes of 5 µm and 10 µm, whereas it is overestimated at a pixel size of 20 µm. **b** Tb.N is underestimated for lower resolutions. This effect is most pronounced at a young age, where structures are relatively small. **c** Tb.Th is overestimated for lower resolutions. At a pixel size of 20 µm differences in trabecular size are unnoticed, since a pixel equals the size of the mean trabecular thickness. **d** Tb.Sp is sparsely affected by decreasing pixel size. It is overestimated at a young age but shows nearly identical results later on. The inter-trabecular space appears less sensitive to variations in scanning resolution. *Figure created by the author, based on his data.*

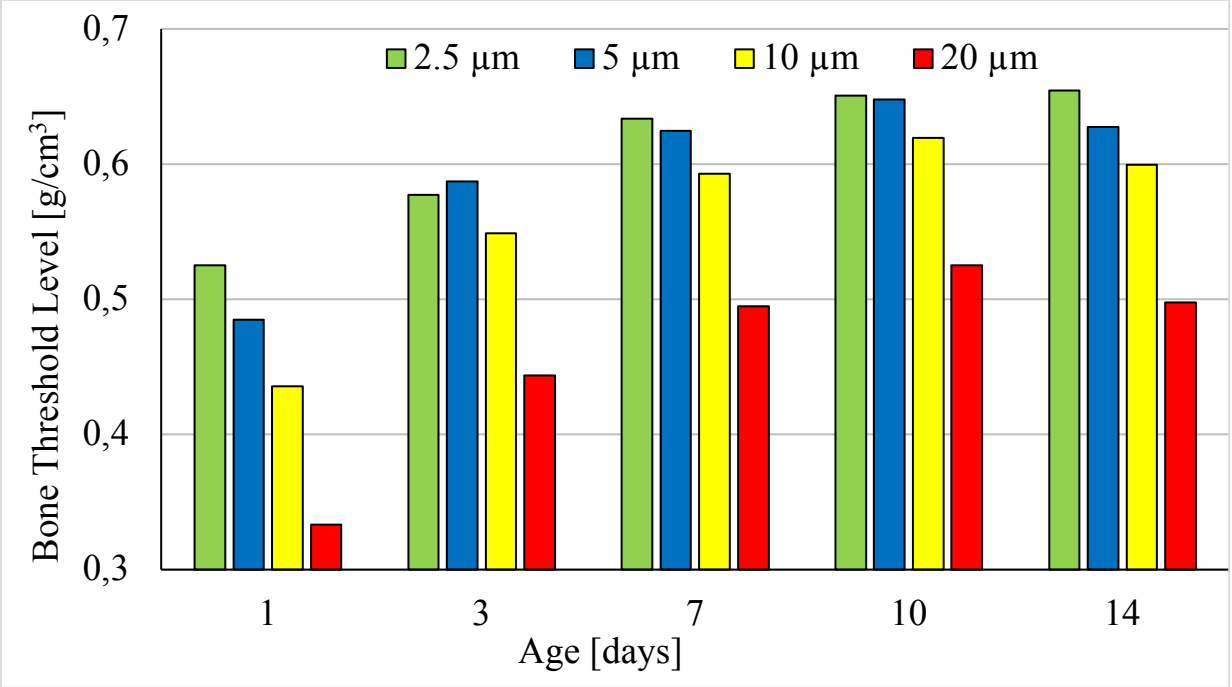

Figure 14: Average threshold level obtained by Otsu's segmentation algorithm in simulated resolutions for pixel sizes of 2.5 µm (original resolution), 5 µm, 10 µm, and 20 µm (scaled VOI in L5 from 19 animals; bone mineral density calibrated to calcium hydroxyapatite phantoms). With increasing age, the mean bone threshold level increases. Lower resolution leads to a lower mean bone threshold level. This is due to edge effects, where neighboring pixels on the bone/background interface are computed into an intermediate, lower resolution when downscaled. A lower threshold results in an overestimation of bone volume (Figure 13). *Figure created by the author, based on his data.*

The effect of different scanning resolutions on the sample population was shown with these simulations, which allowed us to better compare and connect our results to previous studies of age-related changes in cancellous bone of C57BL/6 mice [1,51,52]. General trends in increasing image resolution can be observed as asymptotic functions that approach 'true' size and mineral density.

4. Discussion

A porous mineralized mass present at birth rapidly transforms into a highly sophisticated network of cancellous bone within two weeks. The mineralized network is fully weight-bearing and adapted to the mechanical demands caused by muscle forces, and early locomotion. Cancellous bone development in the early postnatal period has not been studied in this detail before [1]. The presented study provides a detailed 3D analysis and visualization of early physiological cancellous bone evolution, supported and augmented by 2D histology [1].

4.1. Transformation of Cancellous Bone: Going, Going, Gone.

Cancellous bone evolution is a dynamic process, driven by mechanical stimuli, that leads to the transition from a mass of mineralized spicules to a network of trabeculae [1]. Peak bone mass is reached after puberty [57]. A steady-state and eventually a decline in bone mineralization can be observed during aging [51,52,57]: Bones become less elastic and more brittle [108]. Trabeculae decrease in number, loose volume, connectivity, and mechanical competence, resulting in structural weakness and an increased risk of fracture [53,108–112]. Sex and bone type influence the timing and extent of this decline [50,51,53,57].

The relation between the bone structure of several species and their mechanical properties has been outstandingly shown in the life's work of John D. Currey [2]. The importance of locomotion and mechanical stress has been shown during embryogenesis, growth, and aging [31,34,36]. Muscle forces regulate bone shaping, improve mechanical properties, and drive callus ossification in fractures [2,38,113]. The growth plate achieves expansion against mechanical forces [113]. Similar correlations between mechanical stimulation and the formation of bone structure can be observed in the spine of newborn mice: The animals rapidly extend their locomotor abilities in the first few days post-partum, while forming an elaborate bone structure [1,114,115].

Cancellous bone plays an important role in the structural strength of vertebral bodies [2,44,48,116]. Several tests and simulations link bone mechanical properties and architecture [2,33,41,44,62,64,66,116,117]. Yet, no individual morphometric parameter can predict the complex structure-function relationship in the vertebrae [44,66]. The development of fully functional bone under aspects of mechanical stimulation could be simulated in finite element models, based on the presented 3D data. Our results reflect the constant interplay of growing cancellous bone architecture with its mechanical environment during early postnatal growth [1].

4.2. Micro-CT: Importance of Image Resolution, Segmentation, and VOI-Selection

Image resolution should be adapted to a specific sample and research question [76]. It seems easy to aim for the highest possible µCT resolution, but one has to consider possible motion or shrinking artifacts due to long scan durations as well as available computation power and disk space [1,79]. On the other hand, lower scanning resolution results in a lower automated threshold selection, an underestimation of the trabecular number, and overestimation of the trabecular thickness (Figures 13 and 14). These effects of image resolution on quantification, partially match observations made in mice and human cancellous bone [82,87]. Ideally, as achieved in this study, µCT measurements, performed under an appropriate resolution, match those obtained by histomorphometry (Figure 2 [1]) [1,76,90].

Segmentation is a fundamental aspect of automated image analysis since it can systematically and substantially alter the measurements obtained by subsequent analysis (Figure 2) [86]. Different segmentation methods strongly limit direct comparability between published results. The observer independent, automated thresholding is probably the nicest attribute of Otsu's segmentation method. Its application and the comparison with histomorphometry are a major novelty of this work. This algorithm should become the norm in bone analysis software, as it does not assume any fixed/given bone/density threshold and is independent ('objective') [1,85,88].

VOI-selection is another important aspect of comparative µCT studies [1,107]. Different VOIs also limit direct comparability with other studies. By selecting two VOIs in the identical sample, robust measurements were obtained that allowed to compare the growing structures at different timepoints, reliably excluding peripheral growth regions and cortical bone (Figure 1[1], Figure 8, Table 2).

4.3. Phases of Cancellous Bone Formation: Are they Generalizable?

This study describes three distinct phases of early physiological cancellous bone formation in the lumbar spine of a widely employed mouse model [1]. Vertebral bodies offer an excellent study model to map cancellous bone evolution [1]. They contain a relatively large volume of cancellous bone in the centrum (Figure 1[1] and Figure 8). Cancellous bone in the spine is highly sophisticated and adapted to bipedal, quadrupedal locomotion, or swimming [2]. The elaborate bone architecture can be described by an array of histomorphometric parameters along with bone mineral density. These parameters combined, determine the structure's mechanical properties [2,33,39,118,119].

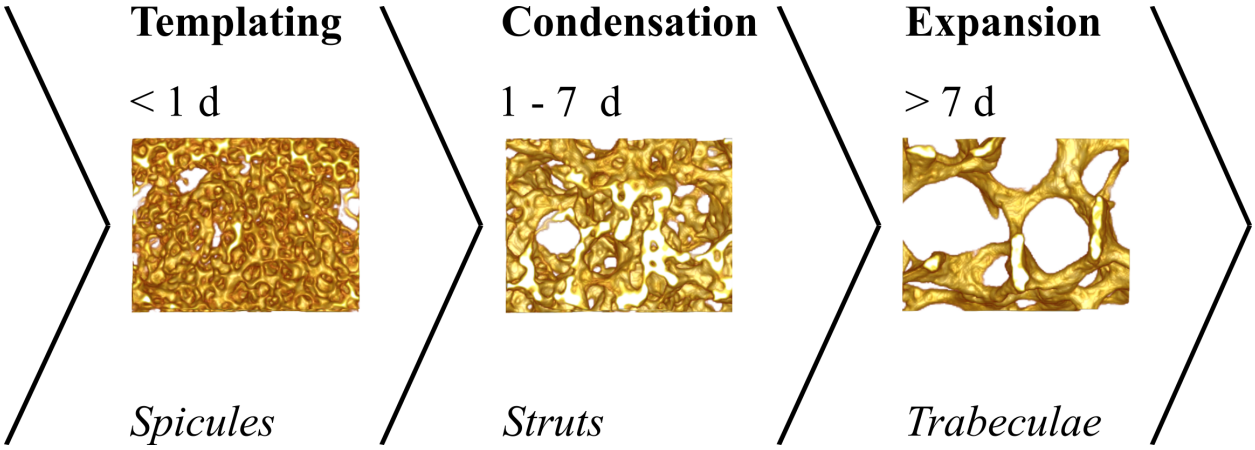

Figure 15: Schematic of three developmental phases in cancellous bone formation: Templating, condensation, and expansion [1]. (i) During a phase of templating, commencing prenatally, a large amount of low-density mineralized material is stored in spicules. (ii) This material then condenses into struts during the first week post-partum. (iii) The formation of early trabeculae is followed by a spatial expansion and remodeling into a mature cancellous bone network. *Figure created by the author, based on his data.*

Bone growth is partially recapitulated during fracture healing [113,120–123]. The cancellous bone formation resembles events that are observed during healing: soft callus formation shows similarities to endochondral ossification [120–122]. The callus only serves as a template for healing and does not result in bone growth. While fracture healing aims to restore structural - thus mechanical capacities, bone growth aims to establish these. The exact healing mechanisms slightly differ with the skeletal site [113,124]. Four stages of fracture healing were identified in the human spine, namely granulation, matrix synthesis, bone formation, and bone (re-) modeling [123]. The last three stages can be related to the phases of bone growth described in this study - yet at a different pace [1]. The differences between the regulation of these processes are of ongoing scientific interest.

The three principal phases of cancellous bone formation described by my work are not unique to the bone formation of the lumbar spine or mice [1]. Such phases have been observed in growing femurs of mice at slightly different timing, where they were described as patterning (day 1 - 7), densification transformation (day 10 - 14), and bone shaping (after 14 days) [49]. A study of cancellous bone development in the human vertebra also showed similar events that led to a refined trabecular architecture: A postnatal decrease in BV/TV, described as a main characteristic of the condensation phase, also takes place in the cancellous bone of the human vertebra [1,56].

Cancellous bone formation in mice and humans may therefore follow a similar, maybe universal pattern.

4.4. Limitations and Outlook

This study analyzes a cohort of 19 female animals of the C57BL/6 mouse strain at five selected time points within the first two weeks post-partum. To compensate for the relatively small sample size, the analysis was extended on three lumbar vertebral bodies per animal [1]. C57BL/6 mice are a widely used study model. However, many details were previously unknown, meriting a full-scale study dedicated just to this animal model as a future reference to other mutation strains or compromised healing scenarios. To eliminate the influence of sex hormones, the study was based on a homogenous, female sample population. In the future, I would like to include male mice and other strains. Polychromatic X-rays in µCT may influence density measurements through beam-hardening effects and subsequent correction algorithms [79,80]. As described in the publication, monochromatic X-rays might improve the precision of density measurements [1].

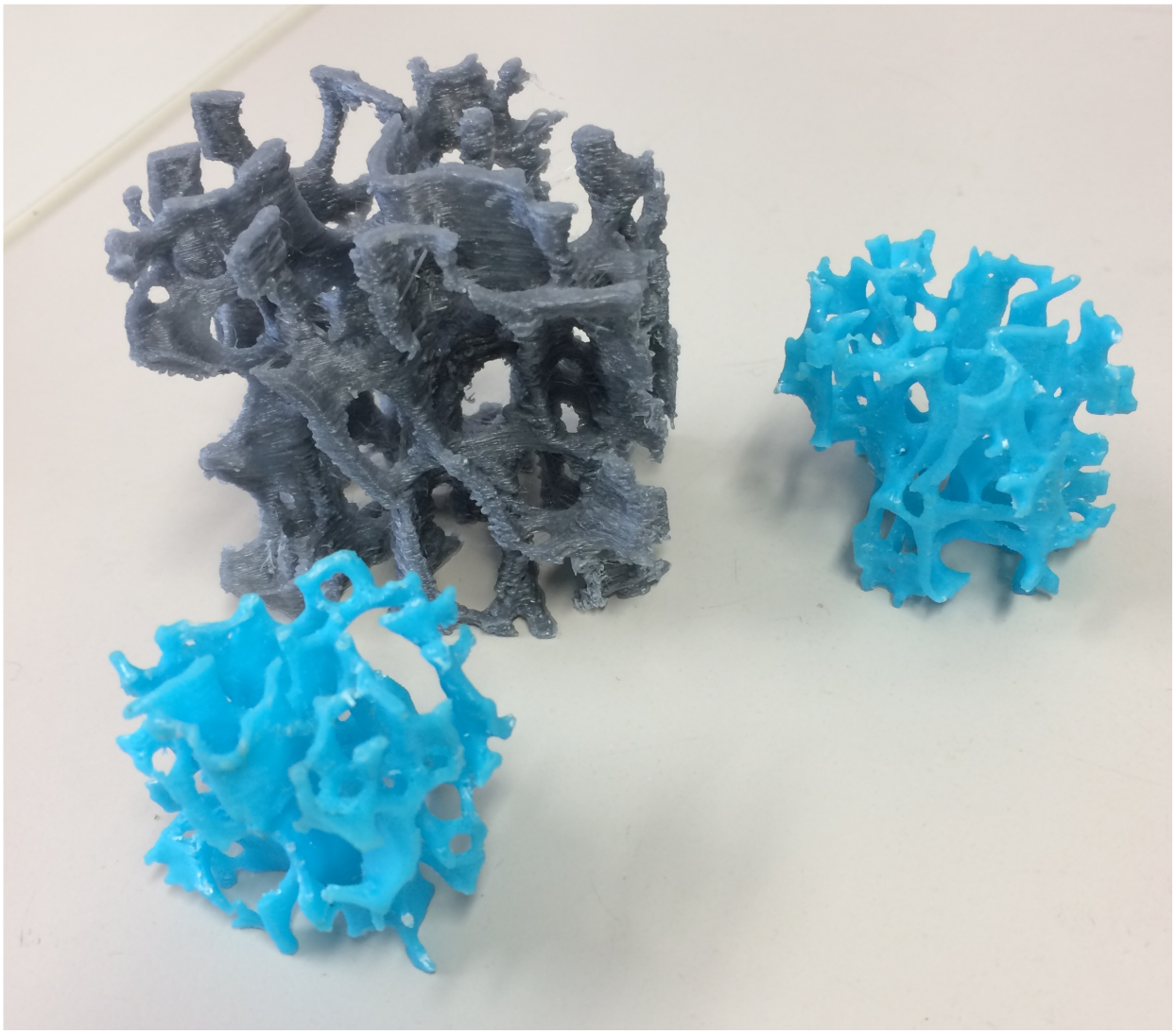

Figure 16: 3D PMMA prints of cancellous bone in the lumbar spine (scaled VOI) in 14-day-old (gray) and 10-day-old (blue) C57BL/6 mice, based on the surface coordinates, computed in Amira (Ver. 5.4.0, Thermo Fisher Scientific, Berlin, Germany). 3D prints may allow repeated mechanical testing of different cancellous bone samples and may be used to design and improve medical implants. *Image taken by the author, based on his data.*

4.5. Conclusions

The following three main conclusions can be drawn from this work: a) A rapid, fundamental morphological transition of the murine lumbar spine architecture takes place in the early days of life. Mineralized spicules and struts condense and form early trabeculae during three distinct phases. The forming structures establish a lattice-like craniocaudal cancellous bone architecture. This results in load-bearing, fully functional cancellous bone within only two weeks. b) The mineralized material is reorganized and shifted from an early deposit to a highly organized, functional structure. c) The observer-independent, 3D-analysis of the architectural evolution quantifies bone growth in a murine model and provides a baseline for physiological cancellous bone formation that may serve as the basis for further studies [1].

Several drugs show immediate or indirect effects on bone formation and homeostasis, such as glucocorticoids, non-steroidal anti-inflammatory drugs, proton-pump inhibitors, sex hormones, and nutritional supplements [125–128]. For the majority of drugs and agents, we can only assume their safety from the experience of use. The influence of pharmacological agents on mineralization and bone structure evolution at a young age is still poorly understood. We have no detailed knowledge of the effects on bone metabolism and structure. Possible long-term effects remain unclear. Especially during the early phases of bone growth, a vulnerable phase observed in this study, it can be assumed that certain external factors may have significant long-term effects. Mice offer an important model to investigate such influences on the skeleton.

This work may help standardize studies across different mouse strains, compare differences between male and female mice, and study several influences on early bone formation including mechanical, metabolic, endocrinological as well as pharmacological effects. This may help to better understand structural levels of bone-related diseases, the interaction of bone and implanted biomaterials, external effects such as biological therapy, or closely related scenarios like healing and growth [1].

5. References

1. Zenzes M, Bortel EL, Fratzl P, Mundlos S, Schuetz M, Schmidt H, Duda GN, Witte F, Zaslansky P. Normal trabecular vertebral bone is formed via rapid transformation of mineralized spicules: A high-resolution 3D ex-vivo murine study. Acta Biomater. 2019 Mar 1;86:429–40.
2. Currey JD. Bones: Structure and Mechanics. Princeton University Press; 2002. 464 p.
3. Weiner S, Traub W, Wagner HD. Lamellar bone: structure-function relations. J Struct Biol. 1999 Jun 30;126(3):241–55.
4. Baron R. Anatomy and Ultrastructure of Bone – Histogenesis, Growth and Remodeling. In: De Groot LJ, Beck-Peccoz P, Chrousos G, Dungan K, Grossman A, Hershman JM, Koch C, McLachlan R, New M, Rebar R, Singer F, Vinik A, Weickert MO, editors. Endotext [Internet]. South Dartmouth (MA): MDText.com, Inc.; 2000 [cited 2015 Dec 31]. Available from: http://www.ncbi.nlm.nih.gov/books/NBK279149/
5. Hall BK. Chapter 2 - Bone. In: Bones and Cartilage (Second Edition) [Internet]. San Diego: Academic Press; 2015 [cited 2016 Mar 19]. p. 17–42. Available from: http://www.sciencedirect.com/science/article/pii/B9780124166783000021
6. Hall BK. Chapter 15 - Cells to Make and Cells to Break. In: Hall BK, editor. Bones and Cartilage (Second Edition) [Internet]. San Diego: Academic Press; 2015 [cited 2020 Apr 29]. p. 239–58. Available from: http://www.sciencedirect.com/science/article/pii/B978012416678300015X
7. Huiskes R, Ruimerman R, van Lenthe GH, Janssen JD. Effects of mechanical forces on maintenance and adaptation of form in trabecular bone. Nature. 2000 Jun 8;405(6787):704–6.
8. Erben RG. Hypothesis: Coupling between Resorption and Formation in Cancellous bone Remodeling is a Mechanically Controlled Event. Front Endocrinol. 2015;6:82.
9. Reznikov N, Shahar R, Weiner S. Bone hierarchical structure in three dimensions. Acta Biomater. 2014 Sep;10(9):3815–26.
10. Erben RG. Trabecular and endocortical bone surfaces in the rat: modeling or remodeling? Anat Rec. 1996 Sep;246(1):39–46.
11. Willie BM, Zimmermann EA, Vitienes I, Main RP, Komarova SV. Bone adaptation: Safety factors and load predictability in shaping skeletal form. Bone. 2020 Feb 1;131:115114.
12. Hautier L, Charles C, Asher RJ, Gaunt SJ. Ossification sequence and genetic patterning in the mouse axial skeleton. J Exp Zoolog B Mol Dev Evol. 2014 Dec;322(8):631–42.
13. Theiler K. The House Mouse [Internet]. Berlin, Heidelberg: Springer Berlin Heidelberg; 1989 [cited 2016 Mar 19]. Available from: http://link.springer.com/10.1007/978-3-642-88418-4
14. Kaufman MH. The Atlas of Mouse Development. Academic Press; 1992. 536 p.
15. Mackie EJ, Ahmed YA, Tatarczuch L, Chen K-S, Mirams M. Endochondral ossification: How cartilage is converted into bone in the developing skeleton. Int J Biochem Cell Biol. 2008;40(1):46–62.
16. Dahia CL, Mahoney EJ, Durrani AA, Wylie C. Intercellular signaling pathways active during and after growth and differentiation of the lumbar vertebral growth plate. Spine. 2011 Jun 15;36(14):1071–80.
17. Shu C, Smith SS, Little CB, Melrose J. Comparative immunolocalisation of perlecan, heparan sulphate, fibroblast growth factor-18, and fibroblast growth factor receptor-3 and their prospective roles in chondrogenic and osteogenic development of the human foetal spine. Eur Spine J Off Publ Eur Spine Soc Eur Spinal Deform Soc Eur Sect Cerv Spine Res Soc. 2013 Aug;22(8):1774–84.
18. Ortega N, Behonick DJ, Werb Z. Matrix remodeling during endochondral ossification. Trends Cell Biol. 2004 Feb;14(2):86–93.
19. Mahamid J, Sharir A, Gur D, Zelzer E, Addadi L, Weiner S. Bone mineralization proceeds through intracellular calcium phosphate loaded vesicles: a cryo-electron microscopy study. J Struct Biol. 2011 Jun;174(3):527–35.
20. Streeter GL. Developmental horizons in human embryos; a review of the histogenesis of cartilage and bone. Contrib Embryol. 1949 Feb;33(213–221):149–68.
21. Hall BK, Miyake T. Divide, accumulate, differentiate: cell condensation in skeletal development revisited. Int J Dev Biol. 2004 Sep 1;39(6):881–93.

22. Wilson R, Norris EL, Brachvogel B, Angelucci C, Zivkovic S, Gordon L, Bernardo BC, Stermann J, Sekiguchi K, Gorman JJ, Bateman JF. Changes in the Chondrocyte and Extracellular Matrix Proteome during Post-natal Mouse Cartilage Development. Mol Cell Proteomics MCP [Internet]. 2012 Jan [cited 2016 Mar 19];11(1). Available from: http://www.ncbi.nlm.nih.gov/pmc/articles/PMC3270109/

23. Karsenty G, Wagner EF. Reaching a genetic and molecular understanding of skeletal development. Dev Cell. 2002 Apr;2(4):389–406.

24. Haimov H, Shimoni E, Brumfeld V, Shemesh M, Varsano N, Addadi L, Weiner S. Mineralization pathways in the active murine epiphyseal growth plate. Bone. 2020 Jan 1;130:115086.

25. Hall BK. Chapter 13 - Dedifferentiation of Chondrocytes and Endochondral Ossification. In: Bones and Cartilage (Second Edition) [Internet]. San Diego: Academic Press; 2015 [cited 2016 Mar 19]. p. 199–218. Available from: http://www.sciencedirect.com/science/article/pii/B9780124166783000136

26. Kerschnitzki M, Wagermaier W, Roschger P, Seto J, Shahar R, Duda GN, Mundlos S, Fratzl P. The organization of the osteocyte network mirrors the extracellular matrix orientation in bone. J Struct Biol. 2011 Feb;173(2):303–11.

27. Seeman E. Periosteal bone formation--a neglected determinant of bone strength. N Engl J Med. 2003 Jul 24;349(4):320–3.

28. Hall BK. Chapter 31 - Growth and Morphogenesis of Long Bones. In: Hall BK, editor. Bones and Cartilage (Second Edition) [Internet]. San Diego: Academic Press; 2015 [cited 2020 Mar 6]. p. 487–502. Available from: http://www.sciencedirect.com/science/article/pii/B9780124166783000318

29. Hall BK. Chapter 5 - Intermediate Tissues. In: Bones and Cartilage (Second Edition) [Internet]. San Diego: Academic Press; 2015 [cited 2016 Mar 19]. p. 79–97. Available from: http://www.sciencedirect.com/science/article/pii/B9780124166783000057

30. Roschger P, Grabner BM, Rinnerthaler S, Tesch W, Kneissel M, Berzlanovich A, Klaushofer K, Fratzl P. Structural development of the mineralized tissue in the human L4 vertebral body. J Struct Biol. 2001 Nov;136(2):126–36.

31. Sharir A, Stern T, Rot C, Shahar R, Zelzer E. Muscle force regulates bone shaping for optimal load-bearing capacity during embryogenesis. Dev Camb Engl. 2011 Aug;138(15):3247–59.

32. Wolff J. Das Gesetz der Transformation der Knochen: Hirschwald, Berlin 1892 - Reprint 300 Seiten - Mit vier Nachworten und historischen Dokumenten - ZVAB - Wolff, Julius [Internet]. [cited 2020 Jan 18]. Available from: https://www.zvab.com/9783868056488/Gesetz-Transformation-Knochen-Hirschwald-Berlin-3868056483/plp

33. Wood Z, Lynn L, Nguyen JT, Black MA, Patel M, Barak MM. Are we crying Wolff? 3D printed replicas of trabecular bone structure demonstrate higher stiffness and strength during off-axis loading. Bone. 2019 Oct 1;127:635–45.

34. Shwartz Y, Farkas Z, Stern T, Aszódi A, Zelzer E. Muscle contraction controls skeletal morphogenesis through regulation of chondrocyte convergent extension. Dev Biol. 2012 Oct 1;370(1):154–63.

35. Hall BK. Chapter 30 - Initiating Skeletal Growth. In: Hall BK, editor. Bones and Cartilage (Second Edition) [Internet]. San Diego: Academic Press; 2015 [cited 2020 Mar 6]. p. 475–86. Available from: http://www.sciencedirect.com/science/article/pii/B9780124166783000306

36. Shwartz Y, Blitz E, Zelzer E. One load to rule them all: mechanical control of the musculoskeletal system in development and aging. Differ Res Biol Divers. 2013 Oct;86(3):104–11.

37. Stern T, Aviram R, Rot C, Galili T, Sharir A, Kalish Achrai N, Keller Y, Shahar R, Zelzer E. Isometric Scaling in Developing Long Bones Is Achieved by an Optimal Epiphyseal Growth Balance. PLoS Biol [Internet]. 2015 Aug 4 [cited 2016 Jan 12];13(8). Available from: http://www.ncbi.nlm.nih.gov/pmc/articles/PMC4524611/

38. Nowlan NC, Bourdon C, Dumas G, Tajbakhsh S, Prendergast PJ, Murphy P. Developing bones are differentially affected by compromised skeletal muscle formation. Bone. 2010 May;46(5):1275–85.

39. Seeman E, Delmas PD. Bone quality--the material and structural basis of bone strength and fragility. N Engl J Med. 2006 May 25;354(21):2250–61.

40. Miller LM, Little W, Schirmer A, Sheik F, Busa B, Judex S. Accretion of Bone Quantity and Quality in the Developing Mouse Skeleton. J Bone Miner Res. 2007 Jul 1;22(7):1037–45.

41. Tommasini SM, Wearne SL, Hof PR, Jepsen KJ. Percolation theory relates corticocancellous architecture to mechanical function in vertebrae of inbred mouse strains. Bone. 2008 Apr;42(4):743–50.

42. Fyhrie DP, Schaffler MB. Failure mechanisms in human vertebral cancellous bone. Bone. 1994 Feb;15(1):105–9.

43. Burr DB. Stress concentrations and bone microdamage: John Currey's contributions to understanding the initiation and arrest of cracks in bone. Bone. 2019 Oct 1;127:517–25.

44. Barak MM, Weiner S, Shahar R. The contribution of trabecular bone to the stiffness and strength of rat lumbar vertebrae. Spine. 2010 Oct 15;35(22):E1153-1159.

45. Eswaran SK, Gupta A, Adams MF, Keaveny TM. Cortical and trabecular load sharing in the human vertebral body. J Bone Miner Res Off J Am Soc Bone Miner Res. 2006 Feb;21(2):307–14.

46. Fields AJ, Eswaran SK, Jekir MG, Keaveny TM. Role of trabecular microarchitecture in whole-vertebral body biomechanical behavior. J Bone Miner Res Off J Am Soc Bone Miner Res. 2009 Sep;24(9):1523–30.

47. Roux J-P, Wegrzyn J, Arlot ME, Guyen O, Delmas PD, Chapurlat R, Bouxsein ML. Contribution of trabecular and cortical components to biomechanical behavior of human vertebrae: an ex vivo study. J Bone Miner Res Off J Am Soc Bone Miner Res. 2010 Feb;25(2):356–61.

48. Ito M, Nishida A, Koga A, Ikeda S, Shiraishi A, Uetani M, Hayashi K, Nakamura T. Contribution of trabecular and cortical components to the mechanical properties of bone and their regulating parameters. Bone. 2002 Sep;31(3):351–8.

49. Bortel EL, Duda GN, Mundlos S, Willie BM, Fratzl P, Zaslansky P. Long bone maturation is driven by pore closing: A quantitative tomography investigation of structural formation in young C57BL/6 mice. Acta Biomater. 2015 Aug;22:92–102.

50. Ferguson VL, Ayers RA, Bateman TA, Simske SJ. Bone development and age-related bone loss in male C57BL/6J mice. Bone. 2003 Sep;33(3):387–98.

51. Glatt V, Canalis E, Stadmeyer L, Bouxsein ML. Age-Related Changes in Trabecular Architecture Differ in Female and Male C57BL/6J Mice. J Bone Miner Res. 2007 Aug 1;22(8):1197–207.

52. Buie HR, Moore CP, Boyd SK. Postpubertal architectural developmental patterns differ between the L3 vertebra and proximal tibia in three inbred strains of mice. J Bone Miner Res Off J Am Soc Bone Miner Res. 2008 Dec;23(12):2048–59.

53. Halloran BP, Ferguson VL, Simske SJ, Burghardt A, Venton LL, Majumdar S. Changes in Bone Structure and Mass With Advancing Age in the Male C57BL/6J Mouse. J Bone Miner Res. 2002 Jun 1;17(6):1044–50.

54. Willie BM, Birkhold AI, Razi H, Thiele T, Aido M, Kruck B, Schill A, Checa S, Main RP, Duda GN. Diminished response to in vivo mechanical loading in trabecular and not cortical bone in adulthood of female C57Bl/6 mice coincides with a reduction in deformation to load. Bone. 2013 Aug 1;55(2):335–46.

55. Bar-Shira-Maymon B, Coleman R, Cohen A, Steinhagen-Thiessen E, Silbermann M. Age-related bone loss in lumbar vertebrae of CW-1 female mice: a histomorphometric study. Calcif Tissue Int. 1989 Jan;44(1):36–45.

56. Acquaah F, Robson Brown KA, Ahmed F, Jeffery N, Abel RL. Early Trabecular Development in Human Vertebrae: Overproduction, Constructive Regression, and Refinement. Front Endocrinol [Internet]. 2015 May 1 [cited 2016 Jan 17];6. Available from: http://www.ncbi.nlm.nih.gov/pmc/articles/PMC4458883/

57. Richman C, Kutilek S, Miyakoshi N, Srivastava AK, Beamer WG, Donahue LR, Rosen CJ, Wergedal JE, Baylink DJ, Mohan S. Postnatal and Pubertal Skeletal Changes Contribute Predominantly to the Differences in Peak Bone Density Between C3H/HeJ and C57BL/6J Mice. J Bone Miner Res. 2001 Feb 1;16(2):386–97.

58. Sharir A, Milgram J, Dubnov-Raz G, Zelzer E, Shahar R. A temporary decrease in mineral density in perinatal mouse long bones. Bone. 2013 Jan;52(1):197–205.

59. Jerome C, Hoch B. 5 - Skeletal System. In: Treuting PM, Dintzis SM, editors. Comparative Anatomy and Histology [Internet]. San Diego: Academic Press; 2012 [cited 2018 Mar 25]. p. 53–70. Available from: https://www.sciencedirect.com/science/article/pii/B9780123813619000056

60. Paavola LG, Wilson DB, Center EM. Histochemistry of the developing notochord, perichordal sheath and vertebrae in Danforth's short-tail (Sd) and normal C57BL/6 mice. Development. 1980 Feb 1;55(1):227–45.

61. Murray EJ, Song MK, Laird EC, Murray SS. Strain-dependent differences in vertebral bone mass, serum osteocalcin, and calcitonin in calcium-replete and -deficient mice. Proc Soc Exp Biol Med Soc Exp Biol Med N Y N. 1993 May;203(1):64–73.

62. Razi H, Birkhold AI, Zaslansky P, Weinkamer R, Duda GN, Willie BM, Checa S. Skeletal maturity leads to a reduction in the strain magnitudes induced within the bone: a murine tibia study. Acta Biomater. 2015 Feb;13:301–10.

63. Brodt MD, Ellis CB, Silva MJ. Growing C57Bl/6 mice increase whole bone mechanical properties by increasing geometric and material properties. J Bone Miner Res Off J Am Soc Bone Miner Res. 1999 Dec;14(12):2159–66.

64. Alwood JS, Yumoto K, Mojarrab R, Limoli CL, Almeida E a. C, Searby ND, Globus RK. Heavy ion irradiation and unloading effects on mouse lumbar vertebral microarchitecture, mechanical properties and tissue stresses. Bone. 2010 Aug;47(2):248–55.

65. Mundlos S, Olsen BR. Heritable diseases of the skeleton. Part I: Molecular insights into skeletal development-transcription factors and signaling pathways. FASEB J. 1997 Feb 1;11(2):125–32.

66. Tommasini SM, Morgan TG, van der Meulen MC, Jepsen KJ. Genetic Variation in Structure-Function Relationships for the Inbred Mouse Lumbar Vertebral Body. J Bone Miner Res. 2005 May 1;20(5):817–27.

67. Kim J-H, Singhal V, Biswal S, Thimmulappa RK, DiGirolamo DJ. Nrf2 is required for normal postnatal bone acquisition in mice. Bone Res. 2014;2:14033.

68. Juneja SC, Vonica A, Zeiss C, Lezon-Geyda K, Yatsula B, Sell DR, Monnier VM, Lin S, Ardito T, Eyre D, Reynolds D, Yao Z, Awad HA, Yu H, Wilson M, Honnons S, Boyce BF, Xing L, Zhang Y, Perkins AS. Deletion of Mecom in mouse results in early-onset spinal deformity and osteopenia. Bone. 2014 Mar;60:148–61.

69. Weidenreich F. Z. Anat. Entwickl. Gesch. Knochenstudien 1 Teil Übver Aufbau Entwickl Knochens Den Charakter Knochengewebes. 1923 März;(69):382–466.

70. Willbold E, Witte F. Histology and research at the hard tissue-implant interface using Technovit 9100 New embedding technique. Acta Biomater. 2010 Nov;6(11):4447–55.

71. Dempster DW, Compston JE, Drezner MK, Glorieux FH, Kanis JA, Malluche H, Meunier PJ, Ott SM, Recker RR, Parfitt AM. Standardized Nomenclature, Symbols, and Units for Bone Histomorphometry: A 2012 Update of the Report of the ASBMR Histomorphometry Nomenclature Committee. J Bone Miner Res Off J Am Soc Bone Miner Res. 2013 Jan;28(1):2–17.

72. Aescht E, Büchl-Zimmermann S, Burmester A, Dänhardt-Pfeiffer S, Desel C, Hamers C, Jach G, Kässens M, Makovitzky J, Mulisch M, Nixdorf-Bergweiler B, Pütz D, Riedelsheimer B, van den Boom F, Wegerhoff R, Welsch U. Romeis Mikroskopische Technik [Internet]. Mulisch M, Welsch U, editors. Heidelberg: Spektrum Akademischer Verlag; 2010 [cited 2016 Mar 19]. Available from: http://link.springer.com/10.1007/978-3-8274-2254-5

73. Currey JD, Brear K, Zioupos P, Reilly GC. Effect of formaldehyde fixation on some mechanical properties of bovine bone. Biomaterials. 1995;16(16):1267–71.

74. Fonseca AA, Cherubini K, Veeck EB, Ladeira RS, Carapeto LP. Effect of 10% formalin on radiographic optical density of bone specimens. Dentomaxillofacial Radiol. 2008 Mar 1;37(3):137–41.

75. Feldkamp LA, Goldstein SA, Parfitt MA, Jesion G, Kleerekoper M. The direct examination of three-dimensional bone architecture in vitro by computed tomography. J Bone Miner Res. 1989 Feb 1;4(1):3–11.

76. Bouxsein ML, Boyd SK, Christiansen BA, Guldberg RE, Jepsen KJ, Müller R. Guidelines for assessment of bone microstructure in rodents using micro-computed tomography. J Bone Miner Res Off J Am Soc Bone Miner Res. 2010 Jul;25(7):1468–86.

77. Odgaard A. Three-dimensional methods for quantification of cancellous bone architecture. Bone. 1997 Apr;20(4):315–28.

78. Rüegsegger P, Koller B, Müller R. A microtomographic system for the nondestructive evaluation of bone architecture. Calcif Tissue Int. 1996 Jan;58(1):24–9.

79. Hsieh J. Computed Tomography: Principles, Design, Artifacts, and Recent Advances. SPIE; 2009. 556 p.

80. Fajardo RJ, Cory E, Patel ND, Nazarian A, Laib A, Manoharan RK, Schmitz JE, DeSilva JM, MacLatchy LM, Snyder BD, Bouxsein ML. Specimen size and porosity can introduce error into μCT-based tissue mineral density measurements. Bone. 2009 Jan;44(1):176–84.

81. Peyrin F, Salome M, Cloetens P, Laval-Jeantet AM, Ritman E, Rüegsegger P. Micro-CT examinations of trabecular bone samples at different resolutions: 14, 7 and 2 micron level. Technol Health Care Off J Eur Soc Eng Med. 1998 Dec;6(5–6):391–401.

82. Isaksson H, Töyräs J, Hakulinen M, Aula AS, Tamminen I, Julkunen P, Kröger H, Jurvelin JS. Structural parameters of normal and osteoporotic human trabecular bone are affected differently by microCT image resolution. Osteoporos Int J Establ Result Coop Eur Found Osteoporos Natl Osteoporos Found USA. 2011 Jan;22(1):167–77.

83. Naveh GRS, Brumfeld V, Dean M, Shahar R, Weiner S. Direct microCT imaging of non-mineralized connective tissues at high resolution. Connect Tissue Res. 2014 Feb;55(1):52–60.

84. Kuhn JL, Goldstein SA, Feldkamp LA, Goulet RW, Jesion G. Evaluation of a microcomputed tomography system to study trabecular bone structure. J Orthop Res. 1990 Nov 1;8(6):833–42.

85. Otsu N. A Threshold Selection Method from Gray-Level Histograms. IEEE Trans Syst Man Cybern. 1979 Jan;9(1):62–6.

86. Hara T, Tanck E, Homminga J, Huiskes R. The influence of microcomputed tomography threshold variations on the assessment of structural and mechanical trabecular bone properties. Bone. 2002 Jul;31(1):107–9.

87. Christiansen BA. Effect of micro-computed tomography voxel size and segmentation method on trabecular bone microstructure measures in mice. Bone Rep. 2016 Dec;5:136–40.

88. Rajagopalan S, Lu L, Yaszemski MJ, Robb RA. Optimal segmentation of microcomputed tomographic images of porous tissue-engineering scaffolds. J Biomed Mater Res A. 2005 Dec 15;75(4):877–87.

89. Scherf H, Tilgner R. A new high-resolution computed tomography (CT) segmentation method for trabecular bone architectural analysis. Am J Phys Anthropol. 2009 Sep;140(1):39–51.

90. Müller R, Hahn M, Vogel M, Delling G, Rüegsegger P. Morphometric analysis of noninvasively assessed bone biopsies: comparison of high-resolution computed tomography and histologic sections. Bone. 1996 Mar;18(3):215–20.

91. Müller R, Van Campenhout H, Van Damme B, Van der Perre G, Dequeker J, Hildebrand T, Rüegsegger P. Morphometric Analysis of Human Bone Biopsies: A Quantitative Structural Comparison of Histological Sections and Micro-Computed Tomography. Bone. 1998 Jul;23(1):59–66.

92. Shanbhag AG. Utilization of Information Measure as a Means of Image Thresholding. CVGIP Graph Models Image Process. 1994 Sep 1;56(5):414–9.

93. Prewitt J, Mendelsohn M. The analysis of cell images. In: Annals of the New York Academy of Sciences. 1966. p. 1035–53.

94. Ridler T, Calvard S. Picture Thresholding Using an Iterative Selection Method. IEEE Trans Syst Man Cybern. 1978 Aug;8(8):630–2.

95. Jui-Cheng Yen, Fu-Juay Chang, Shyang Chang. A new criterion for automatic multilevel thresholding. IEEE Trans Image Process. 1995 Mar;4(3):370–8.

96. Doyle W. Operations Useful for Similarity-Invariant Pattern Recognition. J ACM JACM. 1962 Apr 1;9(2):259–267.

97. Movat HZ. Demonstration of all connective tissue elements in a single section; pentachrome stains. AMA Arch Pathol. 1955 Sep;60(3):289–95.

98. Feldkamp L, Davis LC, Kress J. Practical cone-beam algorithm. J Opt Soc Am. 1984 Jun 1;1:612–9.

99. Salmon PL, Ohlsson C, Shefelbine SJ, Doube M. Structure model index does not measure rods and plates in trabecular bone. Bone Res. 2015;162.

100. Harrigan TP, Mann RW. Characterization of microstructural anisotropy in orthotropic materials using a second rank tensor. J Mater Sci. 1984 Mar;19(3):761–7.

101. Ketcham RA, Ryan TM. Quantification and visualization of anisotropy in trabecular bone. J Microsc. 2004 Feb;213(Pt 2):158–71.

102. HILDEBRAND T, RÜEGSEGGER P. Quantification of Bone Microarchitecture with the Structure Model Index. Comput Methods Biomech Biomed Engin. 1997 Jan 1;1(1):15–23.

103. Liu ZQ. Scale space approach to directional analysis of images. Appl Opt. 1991 Apr 10;30(11):1369–73.

104. Doube M, Kłosowski MM, Arganda-Carreras I, Cordelières FP, Dougherty RP, Jackson JS, Schmid B, Hutchinson JR, Shefelbine SJ. BoneJ: free and extensible bone image analysis in ImageJ. Bone. 2010 Dec;47(6):1076–9.

105. Schneider CA, Rasband WS, Eliceiri KW. NIH Image to ImageJ: 25 years of image analysis. Nat Methods. 2012 Jul;9(7):671–5.

106. Schindelin J, Arganda-Carreras I, Frise E, Kaynig V, Longair M, Pietzsch T, Preibisch S, Rueden C, Saalfeld S, Schmid B, Tinevez J-Y, White DJ, Hartenstein V, Eliceiri K, Tomancak P, Cardona A. Fiji - an Open Source platform for biological image analysis. Nat Methods [Internet]. 2012 Jun 28 [cited 2016 Mar 24];9(7). Available from: http://www.ncbi.nlm.nih.gov/pmc/articles/PMC3855844/

107. Lazenby RA, Skinner MM, Kivell TL, Hublin J-J. Scaling VOI size in 3D μCT studies of trabecular bone: a test of the over-sampling hypothesis. Am J Phys Anthropol. 2011 Feb;144(2):196–203.

108. Zioupos P, Kirchner HOK, Peterlik H. Ageing bone fractures: The case of a ductile to brittle transition that shifts with age. Bone. 2020 Feb 1;131:115176.

109. Mosekilde L. Age-related changes in vertebral trabecular bone architecture--assessed by a new method. Bone. 1988;9(4):247–50.

110. Amstrup AK, Jakobsen NFB, Moser E, Sikjaer T, Mosekilde L, Rejnmark L. Association between bone indices assessed by DXA, HR-pQCT and QCT scans in post-menopausal women. J Bone Miner Metab. 2016 Nov 1;34(6):638–45.

111. Mosekilde L. Age-related changes in bone mass, structure, and strength--effects of loading. Z Für Rheumatol. 2000;59 Suppl 1:1–9.

112. Parfitt AM. Age-related structural changes in trabecular and cortical bone: cellular mechanisms and biomechanical consequences. Calcif Tissue Int. 1984;36 Suppl 1:S123-128.

113. Rot C, Stern T, Blecher R, Friesem B, Zelzer E. A Mechanical Jack-like Mechanism Drives Spontaneous Fracture Healing in Neonatal Mice. Dev Cell. 2014 Oct 27;31(2):159–70.

114. König B. Chapter 2.11 - The Behaviour of the House Mouse A2 - Hedrich, Hans J. In: The Laboratory Mouse (Second Edition) [Internet]. Boston: Academic Press; 2012 [cited 2016 Mar 19]. p. 367–81. Available from: http://www.sciencedirect.com/science/article/pii/B9780123820082000167

115. Meer M van der, Baumans V, Hofhuis FMA, Olivier B, Zutphen BFM van. Consequences of gene targeting procedures for behavioural responses and morphological development of newborn mice. Transgenic Res. 2001 Oct 1;10(5):399–408.

116. Christiansen BA, Kopperdahl DL, Kiel DP, Keaveny TM, Bouxsein ML. Mechanical contributions of the cortical and trabecular compartments contribute to differences in age-related changes in vertebral body strength in men and women assessed by QCT-based finite element analysis. J Bone Miner Res Off J Am Soc Bone Miner Res. 2011 May;26(5):974–83.

117. Tanck E, Van Donkelaar CC, Jepsen KJ, Goldstein SA, Weinans H, Burger EH, Huiskes R. The mechanical consequences of mineralization in embryonic bone. Bone. 2004 Jul;35(1):186–90.

118. Borah B, Dufresne TE, Cockman MD, Gross GJ, Sod EW, Myers WR, Combs KS, Higgins RE, Pierce SA, Stevens ML. Evaluation of changes in trabecular bone architecture and mechanical properties of minipig vertebrae by three-dimensional magnetic resonance microimaging and finite element modeling. J Bone Miner Res Off J Am Soc Bone Miner Res. 2000 Sep;15(9):1786–97.

119. Currey JD, Brear K, Zioupos P. Strain rate dependence of work of fracture tests on bone and similar tissues: Reflections on testing methods and mineral content effects. Bone. 2019 Nov 1;128:115038.

120. Vortkamp A, Pathi S, Peretti GM, Caruso EM, Zaleske DJ, Tabin CJ. Recapitulation of signals regulating embryonic bone formation during postnatal growth and in fracture repair. Mech Dev. 1998 Feb;71(1–2):65–76.

121. Ferguson C, Alpern E, Miclau T, Helms JA. Does adult fracture repair recapitulate embryonic skeletal formation? Mech Dev. 1999 Sep 1;87(1–2):57–66.

122. Gerstenfeld LC, Cullinane DM, Barnes GL, Graves DT, Einhorn TA. Fracture healing as a post-natal developmental process: Molecular, spatial, and temporal aspects of its regulation. J Cell Biochem. 2003 Apr 1;88(5):873–84.

123. Diamond TH, Clark WA, Kumar SV. Histomorphometric analysis of fracture healing cascade in acute osteoporotic vertebral body fractures. Bone. 2007 Mar;40(3):775–80.

124. Sandberg OH, Aspenberg P. Inter-trabecular bone formation: a specific mechanism for healing of cancellous bone. Acta Orthop. 2016 Sep 2;87(5):459–65.

125. Briot K. Bone and glucocorticoids. Ann Endocrinol. 2018 Jun;79(3):115–8.

126. Güler-Yüksel M, Hoes JN, Bultink IEM, Lems WF. Glucocorticoids, Inflammation and Bone. Calcif Tissue Int. 2018;102(5):592–606.

127. Lisowska B, Kosson D, Domaracka K. Positives and negatives of nonsteroidal anti-inflammatory drugs in bone healing: the effects of these drugs on bone repair. Drug Des Devel Ther. 2018 Jun 21;12:1809–14.

128. Martiniakova M, Sarocka A, Babosova R, Galbavy D, Kapusta E, Goc Z, Formicki G, Omelka R. Bone microstructure of mice after prolonged taurine treatment. Physiol Res. 2019 30;68(3):519–23.

129. Lorensen WE, Cline HE. Marching cubes: A high resolution 3D surface construction algorithm. Proc 14th Annu Conf Comput Graph Interact Tech. 1987 Aug 1;163–169.

130. Hildebrand T, Rüegsegger P. A new method for the model-independent assessment of thickness in three-dimensional images. J Microsc. 1997 Jan 1;185(1):67–75.

131. Dougherty R, Kunzelmann K-H. Computing Local Thickness of 3D Structures with ImageJ. Microsc Microanal. 2007 Aug;13(Supplement S02):1678–1679.

132. Parfitt AM, Mathews CH, Villanueva AR, Kleerekoper M, Frame B, Rao DS. Relationships between surface, volume, and thickness of iliac trabecular bone in aging and in osteoporosis. Implications for the microanatomic and cellular mechanisms of bone loss. J Clin Invest. 1983 Oct;72(4):1396–409.

133. Buie HR, Campbell GM, Klinck RJ, MacNeil JA, Boyd SK. Automatic segmentation of cortical and trabecular compartments based on a dual threshold technique for in vivo micro-CT bone analysis. Bone. 2007 Oct;41(4):505–15.

Eidesstattliche Versicherung

„Ich, Michael Zenzes, versichere an Eides statt durch meine eigenhändige Unterschrift, dass ich die vorgelegte Dissertation mit dem Thema: „*High-Resolution 3D-Characterization Reveals Distinct Phases of Cancellous Bone Formation in the Growing Murine Lumbar Spine*“ selbstständig und ohne nicht offengelegte Hilfe Dritter verfasst und keine anderen als die angegebenen Quellen und Hilfsmittel genutzt habe. Alle Stellen, die wörtlich oder dem Sinne nach auf Publikationen oder Vorträgen anderer Autoren beruhen, sind als solche in korrekter Zitierung kenntlich gemacht. Die Abschnitte zu Methodik (insbesondere praktische Arbeiten, Laborbestimmungen, statistische Aufarbeitung) und Resultaten (insbesondere Abbildungen, Graphiken und Tabellen) werden von mir verantwortet.

Meine Anteile an etwaigen Publikationen zu dieser Dissertation entsprechen denen, die in der untenstehenden gemeinsamen Erklärung mit dem Betreuer, angegeben sind. Für sämtliche im Rahmen der Dissertation entstandenen Publikationen wurden die Richtlinien des ICMJE (International Committee of Medical Journal Editors) zur Autorenschaft eingehalten. Ich erkläre ferner, dass mir die Satzung der Charité – Universitätsmedizin Berlin zur Sicherung Guter Wissenschaftlicher Praxis bekannt ist und ich mich zur Einhaltung dieser Satzung verpflichte.

Weiterhin versichere ich, dass ich diese Dissertation weder in gleicher noch in ähnlicher Form bereits an einer anderen Fakultät eingereicht habe. Es handelt sich bei der Dissertation nicht um eine Abschrift der Publikation.

Die Bedeutung dieser eidesstattlichen Versicherung und die strafrechtlichen Folgen einer unwahren eidesstattlichen Versicherung (§156,161 des Strafgesetzbuches) sind mir bekannt und bewusst.“

Datum

_____

Michael Zenzes

Individual Contributions for the Publication

Publication: Zenzes M., Bortel EL, Fratzl P, Mundlos S, Schuetz M, Schmidt H, Duda GN, Witte F, Zaslansky P, Normal trabecular vertebral bone is formed via rapid transformation of mineralized spicules: a high-resolution 3D ex-vivo murine study, Acta Biomaterialia, Volume 86, 1 March 2019, Pages 429-440; https://doi.org/10.1016/j.actbio.2018.12.050

Zenzes M: Conceptualization of the research project, together with Witte F and Zaslansky P; Development of the research question and project design; literature survey and review (Section 1 and 4, References); selection of methodology; planning and performance of experiments: microsurgery, histological preparation and analysis and interpretation, µCT-scanning (Section 2, Fig. 1-2); data acquisition, analysis, evaluation and interpretation (Table 1, Fig. 1 - 6, Section 3); lead author of the publication: manuscript drafting and revision; author of the published version; corresponding author during the publication process; abstract, statement of significance, sections 1 - 4; figure and table design and execution (Fig. 1 - 6; Table 1, Supplementary Fig.1, Video 1 and 2), accountable for all aspect of the work related to accuracy and integrity.

Bortel EL: Scientific and technical advice in the early phase of project design; introduction to µCT methodology; critical revision and editing of the manuscript, final approval of the published version; collection of the whole-body weight of samples; Fig. 3c and Section 2.3.

Fratzl P: Mentoring and scientific advice regarding sample preparation for histological analysis, especially assessment of bone mineral density. Suggestion of literature, review of the manuscript. Critical revision, discussion and final approval of the published version: Fig. 6b and Section 4.5.

Mundlos S: Mentoring, provision of samples; interpretation of clinical context; discussion of outlook and future applications; review of the manuscript and final approval of the published version, Section 2.1.

Schuetz M: Mentoring and scientific advice regarding clinical implications. Final approval of the published version. Poster DKOU, 2017; Section 4.6.

Schmidt H: Mentoring and scientific advice, review of the manuscript, final approval of the published version. Section 1.

Duda GN: Mentoring and scientific advice, provision of facilities in the Julius Wolff Institute, review of the manuscript, final approval of the published version. Section 1.

Witte F: Conceptualization of the research project together with Zenzes M and Zaslansky P; mentoring, scientific advice and troubleshooting especially regarding histological sample

preparation, staining, as well as evaluation and interpretation of histological data. Provision of facilities and supply of materials; critical revision, discussion and final approval of the published version. Co-funding of the conference presentation (Suzhou, China 2016) and research project. Fig. 2, Table 1, Sections 2.4 and 3.1.

Zaslansky P: Conceptualization of the research project, together with Zenzes M and Witte F, main mentor and scientific advisor during the entire research project, publishing- and revision process, scientific advice for the applied methodology (especially μCT imaging) analysis and interpretation of the data; review of the visualization; critical revision, discussion and editing of the manuscript, final approval of the published version. Second corresponding author after the publication process; Co-funding of the conference presentation (Suzhou, China 2016), Poster for the DKOU 2017 and research project. Sections 1 - 4, Fig. 1-2.

Date:

_____

Michael Zenzes

Excerpt from the Journal Summary List

Journal Data Filtered By: **Selected JCR Year: 2017** Selected Editions: SCIE,SSCI
Selected Categories: **"ENGINEERING, BIOMEDICAL"** Selected Category Scheme: WoS

Gesamtanzahl: 78 Journale

Rank	Full Journal Title	Total Cites	Journal Impact Factor	Eigenfactor Score
1	BIOMATERIALS	108,908	8.806	0.114670
2	Annual Review of Biomedical Engineering	4,653	8.788	0.006260
3	Biofabrication	2,758	6.838	0.005720
4	Acta Biomaterialia	30,640	6.383	0.049410
5	IEEE TRANSACTIONS ON MEDICAL IMAGING	17,837	6.131	0.024200
6	Advanced Healthcare Materials	6,465	5.609	0.019660
7	MEDICAL IMAGE ANALYSIS	6,383	5.356	0.011900
8	CLINICAL ORAL IMPLANTS RESEARCH	14,065	4.305	0.016880
9	IEEE TRANSACTIONS ON BIOMEDICAL ENGINEERING	21,496	4.288	0.023780
10	Journal of Tissue Engineering and Regenerative Medicine	3,963	4.089	0.006640
11	IEEE TRANSACTIONS ON NEURAL SYSTEMS AND REHABILITATION ENGINEERING	5,647	3.972	0.008260
12	Journal of Neural Engineering	5,551	3.920	0.009750
13	Journal of NeuroEngineering and Rehabilitation	4,325	3.865	0.009120
14	EUROPEAN CELLS & MATERIALS	3,115	3.667	0.004290
15	IEEE Transactions on Biomedical Circuits and Systems	2,543	3.500	0.005780
16	ANNALS OF BIOMEDICAL ENGINEERING	10,881	3.405	0.017170
17	JOURNAL OF BIOMEDICAL MATERIALS RESEARCH PART B-APPLIED BIOMATERIALS	8,513	3.373	0.008410
18	Journal of the Mechanical Behavior of Biomedical Materials	7,713	3.239	0.017270
19	JOURNAL OF BIOMEDICAL MATERIALS RESEARCH PART A	17,464	3.231	0.016510

Published Manuscript

https://doi.org/10.1016/j.actbio.2018.12.050

Supplementary data from [1]

https://doi.org/10.1016/j.actbio.2018.12.050

Curriculum Vitae

Mein Lebenslauf wird aus datenschutzrechtlichen Gründen in der elektronischen Version meiner Arbeit nicht veröffentlicht.

Publications List

Zenzes M. [1], Bortel EL [1,*], Fratzl P [2], Mundlos S [3], Schuetz M [4,&], Schmidt H [1], Duda GN [1], Witte F [5,§], Zaslansky P [1,5], Normal trabecular vertebral bone is formed via rapid transformation of mineralized spicules: a high-resolution 3D ex-vivo murine study, Acta Biomaterialia, available online 31 December 2018, published In Volume 86, 1 March 2019, Pages 429-440, https://doi.org/10.1016/j.actbio.2018.12.050

Authors Affiliations:

[1] Julius Wolff Institute, Charité-Universitätsmedizin Berlin, Augustenburger Platz 1, 13353 Berlin, Germany
[2] Department of Biomaterials, Max Planck Institute of Colloids and Interfaces, Research Campus Golm, 14424 Potsdam, Germany
[3] Institute of Medical and Human Genetics, Charité Universitätsmedizin Berlin, Augustenburger Platz 1, 13353 Berlin, Germany
[4] Center for Musculoskeletal Surgery, Charité Universitätsmedizin Berlin, Augustenburger Platz 1, 13353 Berlin, Germany
[5] Department of preventive and restorative dentistry, Charité Universitätsmedizin Berlin, Assmanshauser Str 4-6, 14197, Berlin, Germany
[&]*Permanent address: Department for Orthopaedics & Trauma, Royal Brisbane and Women's Hospital,* Herston Queensland 4029, Australia
[*]*Present address: XPLORAYTION GmbH, Bismarckstrasse 10-12, 10625 Berlin, Germany*
[§]*Permanent address: botiss biomaterials GmbH Büro Berlin, Ullsteinstraße 108, 12109 Berlin, Germany*

Appendix

A) Specific Abbreviations of 3D-Measurements

see Section 2.3, Fig. 5, Supplementary data [1]

BV/TV **Bone volume to Tissue volume ratio**

Bone volume fraction (BV/TV) or the volume of bone per volume unit, is the number of foreground voxels divided by the total number of voxels [104].

BS/BV **Bone surface to Bone volume ration, specific Bone surface; mm^2/mm^3**

'Specific bone surface' gives a measure of bone surface per volume. Bone volume (BV) is a bone voxel count. To calculate bone surface (BS), a triangular mesh is produced by the marching cubes algorithm. The surface equals the sum of the areas of the triangular mesh [104,129].

DA **Degree of anisotropy**

The 'Degree of anisotropy' gives a measure of orientation. It is based on the mean intercept length (MIL) method: A series of vectors of the same length are drawn originating from a random point. An intercept is counted when a vector crosses the line between foreground and background. The MIL equals the vector length divided by the number of intercepts. A cloud of points is drawn, where each point represents the vector times its mean intercept length. An ellipsoid is fitted to the cloud. Construction of a material anisotropy tensor and eigendecomposition results in eigenvalues which relate to the lengths of the ellipsoid's axes and eigenvectors giving the orientation of the axes. DA is calculated as 1 - smallest eigenvalue / largest eigenvalue. 0 = isotropic, 1 = anisotropic [77,104].

SMI **Structure Model Index**

The structure model index (SMI) aims to quantify the geometry of trabecular structures. It uses the change in BS as volume increases infinitesimally to calculate values: SMI = 0 for plates, 3 for rods and 4 for solid spheres. SMI is of limited use to quantify geometry, since it has negative values for concave surfaces. It is, nevertheless, included in the results of this study because it was commonly used in bone research. Instead one should consider using the ellipsoid factor. [99,102,104]

Tb.Th **Trabecular thickness**

and

Tb.Sp **Trabecular separation**

The thickness is defined as the diameter of the greatest sphere that fits within the trabecular structure. Mean and standard deviation of trabecular thickness (Tb.Th) and trabecular spacing (Tb.Sp) are calculated from pixel values. [104,130,131]

Tb.N **Trabecular number**

The Trabecular number is calculated according to the parallel plate model as (BV/TV)/Tb.Th [71,132].

B) µCT Scanning Protocol

see Section 2.2 [1]

Consistent and reliable image acquisition is necessary for the qualitative comparison of µCT images.

1. Start PC and Skyscan 1172 benchtop µCT.
2. Samples stored in 2 ml 70% EtOH at 4 °C are mounted inside a custom-made specimen holder using two polystyrene rings. Sponges soaked with 70% EtOH ensure a humid atmosphere during the scan.
3. Open specimen chamber and install specimen holder.
4. Close specimen chamber and perform a scout scan.

5. Check:
   Targeted ROI (L3-L5) visible in scout scan?
   Is the sample oriented upright and centered along the craniocaudal axis?
   Does the sample not rotate out of the plane when turning?
   Line Histogram: Detector does not saturate?

6. Load configuration file for all samples:

   X-ray tube voltage 50 keV (198 µA), 0.5 mm aluminum filter, Image acquisition over 360°, image rotation steps of 0.1°, exposure time of 1.45 s, effective pixel size of 2.51 µm.

7. Start the scan with a delay of 30-60 min to allow for thermal calibration and reduction of movement artifacts.
8. Store the sample in a fresh 70% EtOH solution at 4 °C after the scan is completed.

C) Quantification of Cancellous Bone Architecture at 4 Months

see Section 3.2 [1]

A 4-months-old vertebra of a female C57BL/6 mouse was analyzed under the standard protocol. The mean values of L3-L5 are given here. The different results from the larger scaled VOI and the small constant VOI show the morphological differences of the center compared to the rest of the cancellous bone inside the vertebral body at this age.

	Constant VOI Mean	Constant VOI SD	**Scaled VOI Mean**	Scaled VOI SD
BV/TV {%}	13.5	-	17.79	-
Tb.Th {µm}	33.37	*9.38*	34.43	*12.41*
Tb.Sp {µm}	211.23	*60.16*	174.46	*66.32*
Tb.N {mm^{-1}}	4.04	-	5.16	-
BS/BV {mm^2/mm^3}	2.40	-	2.29	-
SMI {}	2.082	-	1.502	-
DA {}	0.70	-	0.71	-

Maximum dimensions of the vertebral bodies L3-L5 in {mm}

	L3	**L4**	**L5**	**MEAN**
Hight	2.40	2.52	2.56	2.49
Width	1.35	1.43	1.40	1.39
Depth	1.07	1.09	1.01	1.06

D) Automated Data Processing to Separate Bone Types

see Sections 1, 3.4.2, 4.5, Fig. 1 [1]

Automated separation of cortical- and cancellous bone in large datasets of long bone implemented as an ImageJ Macro. The number of iterations in the Macro should be adapted to the individual sample type. This macro requires a defined cortical structure to be reliable, therefore, it was not applicable in the youngest samples. Adapted and modified from Buie et al. [133].

Input: A binary image stack filled with cortical and cancellous bone regions.

```
run("Duplicate...", "title=cortical duplicate");
run("Duplicate...", "title=spongiosa duplicate");
run("Duplicate...", "title=corticalMASK duplicate");
run("Duplicate...", "title=spongiosaMASK duplicate");
```

Cortical outlines

```
selectWindow("corticalMASK");
//run("Threshold...");
run("Convert to Mask", "method=Otsu background=Default calculate black");
run("Despeckle", "stack");
run("Dilate", "stack");
run("Dilate", "stack");
run("Erode", "stack");
run("Erode", "stack");
run("Options...", "iterations=1 count=1 black do=[Fill Holes] stack");
```

Spongiosa outlines

```
selectWindow("spongiosaMASK");
//run("Threshold...");
run("Convert to Mask", "method=Otsu background=Default calculate black");
run("Invert", "stack");
imageCalculator("AND create stack", "spongiosaMASK","corticalMASK");
rename("spongiosa2");
run("Options...", "iterations=3 count=1 black do=Open stack");
```

```
run("Options...", "iterations=6 count=1 black do=Close stack");
run("Duplicate...", "title=spongiosa3 duplicate");
run("Divide...", "value=255 stack");
selectWindow("cortical");
imageCalculator("Multiply create stack", "spongiosa3","spongiosa");

imageCalculator("Subtract create stack", "corticalMASK","spongiosa2");
rename("cortexring");
run("Divide...", "value=255 stack");
imageCalculator("Multiply create stack", "cortical","cortexring");
```

E) Microsurgical Sample Preparation

see Section 2.1 [1]

Handling and preparation of the delicate samples at a very young age required attention and prudence to preserve structural integrity. The following protocol was applied to all animals.

1. Animals are taken out of -80 °C freezer and checked for integrity.
2. Animals were weighed.
3. Animals were thawed at 4 °C for 24 hours in a PFA- or EtOH -solution.

   PFA-fixation: thawed in a 4% PBS-buffered PFA solution for 24 hours; washed in fresh PBS solution for 1-2 hours before surgical preparation.
   EtOH-fixation: thawed in 70% EtOH solution, then transferred to fresh 70% EtOH 1-2 hours before surgical preparation.

4. Microsurgical preparation under a 2.5 x magnification stereomicroscope and a cold-light source. The extremities of the animals were fixed with needles in the metacarpal and metatarsal region on a polystyrene board. The specimens were kept irrigated during preparation.
5. An incision was made cranial of the first ribs down to the base of the tail. Skin and fasciae were carefully dissected. Special attention was directed on the preservation of the macro-architecture of the lumbar spine:

   1- 3-day-old animals: paravertebral incision
   7- 14-day-old animals: medial incision

6. Lumbar- and sacral- spine segments were exposed. To detach the sample, cuts were placed above the first ribs, below the first caudal vertebra and 2-3 mm distal of the femoral-acetabular joint. The extracted specimens included the 12th thoracic vertebrae, the six lumbar vertebrae, the pelvis, as well as the femoral head.
7. Samples were labeled and individually stored in 2 ml 70% EtOH solution at 4 °C.

F) Sample Embedding with Technovit 9100 new

see Section 2.4 [1]

Mineralized material is most challenging for histological research. The growing lumbar spine consists of a succession of hard and soft materials of different densities and properties. Also, the very small samples were previously frozen for preservation. To present these delicate structures, a PMMA embedding was applied that allowed the samples to be non-decalcified. Please refer to the user manuals of Kulzer GmbH for further details on Technovit 9100 new.

An intensified dehydration and embedding protocol with more frequent medium changes was applied. To anticipate bending and torsion during the dehydration process, the samples were carefully tied to the histo-box using 1-0 polyfil polyester sutures (Mersilene, Ethicon).

Medium	Duration
70% EtOH	4h /4h / overnight
70% EtOH	4h /4h / overnight
96% EtOH	4h /4h / overnight
96% EtOH	4h /4h / overnight
Isopropyl alcohol	4h /4h / overnight
Isopropyl alcohol	4h /4h / overnight
Xylol	4h /4h / overnight
Xylol	4h /4h / overnight
Pre-Infiltration solution	3 days at 4°C and -0.9 bar
Infiltration solution	7 days
Polymerization	

Samples were embedded in Technovit 9100 new following the manufacturer's protocol. All samples were oriented with the vertebral arches facing the cutting plane.
Samples that showed air enclosures or cracks in the slicing plane were ground and re-embedded to guarantee homogeneous slices.

PMMA blocks were sliced using a Leica SM2500S microtome, which allowed a steady and smooth cutting. Slice thickness was 5 µm.

A cutting-fluid containing 5% TritonX and a mounting-fluid of 70%-EtOH in combination with some drops of a 20% ethanol-based-solution of Butoxyethylacetate showed best results after multiple pre-tests. The slices were transferred to adhesive, silane treated microscope slides (Paul Marienfeld GmbH & Co. KG, Germany). Samples were moistened throughout the whole slicing process.

Especially the 1- and 3-day-old samples showed a strong tendency to lose the mineralized network inside the vertebral bodies and float-off from the silane treated microscope slides during processing. This could successfully be avoided by using pre-treated glass slides, which received a thin gelatine-chromalaun coating to improve adhesion.
Once a sample slice was mounted on a slide, it was covered with PVC foil and filter paper. The slides were dried at 60°C for 2 days under gentle pressure.

Digital images were obtained using a Zeiss Axioskop 2 (Carl Zeiss Microscopy GmbH, Germany) and Axio Vision Image acquisition software.

G) Combined von Kossa / Toluidine Blue Staining

see Section 2.4, Fig. 2 [1]

1.	Removal of PMMA plastic	3x 30 min
2.	Descending alcohol concentration (100% > 70% > a.d.)	2 min each
3.	3% water based $AgNO_3$ solution	10 min
4.	Distilled water	Rinse 3 times
5.	Sodiumcarbonate-Formaldehyde Solution	2 min
6.	Tap water (rinse)	10 min
7.	5% Sodiumthiosulfate-Solution ($Na_2S_2O_3$)	5 min
8.	Tap water (rinse)	10 min
9.	Distilled water	Rinse 5 times
10.	Toluidine Blue O	1-10 min
11.	Distilled water	Rinse quickly
12.	70% EtOH	differentiate
13.	100% EtOH	2 min
14.	100% EtOH	2 min
15.	Xylol	2x 5 min
16.	Cover the sections with Vitroclud	

<u>Staining Results:</u>

Mineralized bone	black
Mineralized Cartilage	dark blue
Cells and soft Tissue	dhades of blue
Cartilage and Mast cell granules	metachromatic shades of blue / violet

H) Movat's Pentachrome Staining

see Section 2.4; Supplementary data [1]

1.	Removal of PMMA plastic	3x 30 min
2.	Descending alcohol concentration (100% > 70% > a.d.)	2 min each
3.	Alcian Blue	10 min
4.	Tab water	5min
5.	Alkalie EtOH (10ml NH_3OH + 90 ml 96% EtOH)	60 min
6.	Tab water (rinse)	10 min
7.	Distilled water	rinse
8.	Weigert's iron hematoxylin	10 min
9.	Tab water (rinse)	10min
10.	Distilled water	2 min
11.	Brilliant Crocein Acid Fuchsin	10-15 min
12.	0,5% Acetic acid	rinse
13.	5% phosphotungstic acid	20 min
14.	0,5% Acetic acid	rinse
15.	100% EtOH (I-III)	2 min each
16.	Saffron du Gatinais	60 min
17.	100% EtOH IV-VI	2 min each
18.	Xylol	2x 5 min
19.	Cover the sections with Vitroclud	

Staining results:

Mineralized bone	bright yellow
Collagen	bright yellow
Mineralized Cartilage	green-blue
Cartilage Tissue	red / yellow
Osteoid	dark red
Elastic fibers	red
Cell nuclei	blue / black
Cytoplasm	shades of red
Glycosaminoglycan	bright blue

Acknowledgements

Ah, love, let us be true
To one another! for the world, which seems
To lie before us like a land of dreams,
So various, so beautiful, so new,
Hath really neither joy, nor love, nor light,
Nor certitude, nor peace, nor help for pain;
And we are here as on a darkling plain
Swept with confused alarms of struggle and flight,
Where ignorant armies clash by night.

Matthew Arnold, 1867.

I would like to thank the lab technicians and IT-experts at the JWI for their patience, optimism, and practical advice. The same applies to the colleagues from my workgroup namely Emely Bortel, Katrein Sauer, and Tom Lindtner, who provided me with stimulating conversations and useful feedback. It was - and is a pleasure working with them. Special thanks to Hadar Zaslansky for the execution of the 3D prints.

I would like to especially thank Prof. Dr. Frank Witte for his kind support, supervision, and funding for this project.
Very special thanks go to my mentor Dr. Paul Zaslansky. His unconditional support, his enthusiastic, unconventional, new approaches turned this research into an enriching experience on a scientific, professional, and personal level. תודה רבה.

Unfortunately, I could not finish this dissertation soon enough to share it with Dr. John Currey, who was noble and patient enough to host me in York to discuss the mouse lumbar spine over tea and sea salt truffles.

Sincere thanks for constant support and motivation belongs to my family and friends. It is a curious coincidence that my father studied the radiographic anatomy of rats - in 2D - for his dissertation. 3 decades later technology allows me to add another dimension to his radiographs. Danke.